

## Perseus ALMA Chemistry Survey (PEACHES). I. The Complex Organic Molecules of Embedded Protostars

YAO-LUN YANG,<sup>1,2</sup> NAMI SAKAI,<sup>2</sup> YICHEN ZHANG,<sup>2</sup> AYA E. HIGUCHI,<sup>3</sup> NADIA M. MURILLO,<sup>2</sup> SHAOSHAN ZENG,<sup>2</sup> ZIWEI ZHANG,<sup>2</sup> MUNEAKI IMAI,<sup>4</sup> TAKESHI SAKAI,<sup>5</sup> ANA LÓPEZ-SEPULCRE,<sup>6</sup> YOKO OYA,<sup>4</sup> YOSHIMASA WATANABE,<sup>7</sup> TOMOYA HIROTA,<sup>3</sup> SATOSHI YAMAMOTO,<sup>4</sup> CECILIA CECCARELLI,<sup>6</sup> AND BERTRAND LEFLOCH<sup>6</sup>

<sup>1</sup>Department of Astronomy, University of Virginia, Charlottesville, VA 22904-4235, USA

<sup>2</sup>RIKEN Cluster for Pioneering Research, Wako-shi, Saitama, 351-0106, Japan

<sup>3</sup>National Astronomical Observatory of Japan, Osawa, Mitaka, Tokyo 181-8588, Japan

<sup>4</sup>Department of Physics, The University of Tokyo, 7-3-1, Hongo, Bunkyo-ku, Tokyo 113-0033, Japan

<sup>5</sup>Department of Communication Engineering and Informatics, Graduate School of Informatics and Engineering,

The University of Electro-Communications, Chofugaoka, Chofu, Tokyo 182-8585, Japan

<sup>6</sup>Univ. Grenoble Alpes, CNRS, Institut de Planétologie et d'Astrophysique de Grenoble (IPAG), F-38000 Grenoble, France

<sup>7</sup>Shibaura Institute of Technology, 3-9-14 Shibaura, Minato-ku, Tokyo 108-8548, Japan

### ABSTRACT

Complex organic molecules at the protostellar phase constrain the chemistry at the warm inner envelope as well as the disk-forming region, which may affect the chemical composition of disks and the planet formation therein. This study introduces an unbiased ALMA chemistry survey toward the Class 0/I protostars in the Perseus molecule cloud (PEACHES) and characterize the statistics of the abundance complex organic molecules. Among the 50 embedded protostars surveyed, 58% have emission of COMs with 56% have CH<sub>3</sub>OH, 32% have HCOOCH<sub>3</sub>, and 40% have N-bearing COMs. The column densities of COMs modeled with LTE radiative transfer correlate with each other and remain correlated with the normalizations of the bolometric luminosities, the bolometric temperature, and the average continuum brightness temperature. The similar chemistry of COMs among a diverse sample hints a universal chemistry of COMs at the embedded phase of star formation. At the same time, the abundance of more complex species, such as HCOOCH<sub>3</sub> and CH<sub>3</sub>OCH<sub>3</sub>, relative to that of less complex species, such as CH<sub>3</sub>OH and CH<sub>3</sub>CN, increases as the inferred gas column density, suggesting a possible enhanced production of more complex species at more embedded sources.

### 1. INTRODUCTION

Planet formation may start during the embedded phase of star formation. In the scenario where planets form from the embedded disks, resulting in substructures, the chemistry of embedded disks may play a significant role for the chemical composition of the forming planets. In the recent years, observations discover the emission of unsaturated complex organic molecules such as carbon-chain molecules (e.g., Sakai & Yamamoto 2013; Sakai et al. 2014; Law et al. 2018) and the saturated complex organic molecules (COMs, Cazaux et al. e.g., 2003; Bottinelli et al. e.g., 2007; Jorgensen et al. e.g., 2020) toward the center of several protostellar cores, indicating that embedded protostars have developed a complex chemistry at the disk-forming region. The saturated organic molecules have single covalent

bonds for all atoms, making them rich in hydrogen, while the unsaturated organic molecules contain double or triple bonds between carbon atoms, making them poor in hydrogen. If the forming planets inherit the chemistry of embedded disks, the abundance of complex organic molecules may implicate future developments of organics on the planets.

Heavier or more complex molecules, such as cyclic-C<sub>3</sub>H<sub>2</sub>, SO, and complex organic molecules (COMs), are in the gas phase at the inner protostellar envelope ( $T \gtrsim 100$  K), which coincidentally corresponds to  $\sim 100$  au for typical low-mass protostars (Yang et al. 2020). Thus, COMs exclusively trace the properties of the inner envelope where a disk may be forming (Aikawa 2013; Sakai et al. 2014). The kinematics of a rotating infalling envelope has been analyzed with the observations of heavier or more complex molecules, such as CH<sub>3</sub>OH and CH<sub>2</sub>DOH for HH 212 (Lee et al. 2017), CS for IRAS 04365+2535 (Sakai et al. 2016) and L483 (Oya et al. 2017), cyclic-C<sub>3</sub>H<sub>2</sub> for L1527 (Sakai et al.

2014), OCS for IRAS 16293–2422 A (Oya et al. 2016), and methanol and HCOOH for B335 (Imai et al. 2019).

While recent observations show several embedded protostars with rich spectra of complex molecules, the occurrence of complex molecules at embedded protostars and its relationship to the star formation process remain poorly understood. Several protostars are rich in COMs but show little emission of long carbon-chain molecules, such as IRAS 16293–2422 (Jørgensen et al. 2016), NGC 1333 IRAS 4A (Bottinelli et al. 2004; Sahu et al. 2019), and B335 (Imai et al. 2016, 2019); some protostars are rich in long carbon-chain molecules but not in COMs, such as L1527 (Sakai et al. 2010) and IRAS 15398–3359 (Sakai et al. 2009). While the bimodal chemical appearance hints a bimodal evolutionary path, the chemical pathways of complex molecules at the embedded protostars remain ill-constrained as a few protostars show the emission of both COMs and long carbon-chain molecules at different scales, such as L483 (Oya et al. 2017). Recent surveys show lack of correlations between COMs and long carbon-chain molecules, suggesting that observational biases may contribute to the apparent bimodal chemistry (Graninger et al. 2016; Higuchi et al. 2018) ([reference](#)).

Perseus molecular cloud is one of the most active nearby star-forming region, which extends  $\sim$ 10 pc on the sky. Infrared and submillimeter surveys reveal more than 400 young stellar objects as well as  $\sim$ 100 dense cores, which contains  $\sim$ 50 Class 0 and I protostars (Hatchell et al. 2005; Jørgensen et al. 2008; Dunham et al. 2013; hereafter the embedded protostars). The Perseus molecular cloud contains star-forming regions in a wide range of environments. The majority of protostars in Perseus are associated with two clusters, NGC 1333 and IC 348. NGC 1333 has significant outflow activity (Plunkett et al. 2013) and a younger age than that of IC 348. The embedded protostars associated with IC 348 lie at the southwest of IC 348 near a prominent outflow, HH 211 (e.g., Lee et al. 2009). Most of other embedded protostars at Perseus are related to L1448, L1455, Bernard 1 (B1), and Bernard 5 (B5). L1448 has active outflows that may regulate the ongoing star formation (Curtis et al. 2010); The lack of Class 0 protostars in L1455 suggest a slightly more evolved protostellar population than in other regions (Hatchell et al. 2007); B1 exhibits rich spectra of deuterated species ([reference](#)). Thus, the Perseus molecular cloud provides the ideal test bed for chemistry in embedded protostars by surveying the protostars within each region and across the entire cloud.

Higuchi et al. (2018) presented a pilot survey of the chemistry in the Perseus embedded protostars with

Nobeyama 45m telescope, which survey all Class 0/I protostars (Hatchell et al. 2007) that have the bolometric luminosity ( $L_{\text{bol}}$ ) greater than  $1 L_{\odot}$  ( $0.7 L_{\odot}$  for protostars in B1 and B5) and the envelope mass greater than  $1 M_{\odot}$ . This pilot survey probes the molecules such as C<sub>2</sub>H, c-C<sub>3</sub>H<sub>2</sub>, and CH<sub>3</sub>OH and find the majority of the sources are neither only rich in CH<sub>3</sub>OH or carbon-chain molecules. They also suggest a possible correlation between the location of sources within the clouds and the chemistry. Other surveys with single-dish telescopes also characterize the COMs abundance at embedded protostars and test the chemical models (e.g., Bergner et al. 2017). Due to the large beam, chemistry survey with single-dish telescopes often more sensitive to COMs in cool temperature (10–20 K), which may not be directly associated with the COMs thermally desorbed from icy grains. Interferometry is crucial for probing the warm COMs at embedded protostars. With 26 embedded protostars from several star-forming regions, Belloche et al. (2020) find CH<sub>3</sub>OH in about half fo the sample as well as other more complex COMs. They also investigate the potential origin of COMs and reveal apparent chemical difference among multiple systems. Despite of the growing sample of COMs detections in embedded protostars, the statistics of COMs occurrence and abundance remain unconstrained due to the biases from the source selection and the limited resolution. To unbiasedly survey the chemistry, we conducted the Perseus ALMA Chemistry Survey (PEACHES) that probes the complex chemistry toward Perseuse embedded protostars. The source selection follows the same criteria as Higuchi et al. (2018) with a few pointing modifications using the results from the VLA Nascent Disk and Multiplicity Survey (VANDAM) of Perseus protostars (Tobin et al. 2016).

Section 2 describes the details of our ALMA observations. Section 3 presents the identification of protostellar sources and the methodology of spectral extraction, line identification and modeling. Section 4 show the detection statistics of COMs and their correlations. Section 5 discusses the implication of the observed COMs abundance to the current understanding of chemistry of COMs at protostellar sources. Finally, Section 6 summarizes the findings of this study.

## 2. OBSERVATIONS

The PEACHES observations were conducted in two ALMA projects (2016.1.01501.S and 2017.1.01462.S; PI: N. Sakai), surveying 37 fields toward the Perseus molecular cloud. Table 1 lists the details about the ALMA projects used in this study. ALMA correlator was configured to have 13 spectral windows (spw) at Band 6,

which have 12 narrow spws with 480 channels and a wide spw with 980 channels. The narrow spws were tuned to observe specific molecular species, such as SiO, CS, CH<sub>3</sub>OH and CH<sub>3</sub>CN, with a spectral resolution of 122 kHz ( $\sim 0.15 \text{ km s}^{-1}$ ), while the wide spw aimed to observe the continuum with a resolution of 0.976 MHz ( $\sim 0.4 \text{ km s}^{-1}$ ). The frequency setup for the two ALMA projects are largely identical except for the wide continuum window (spw04), which shifts by  $\sim 620 \text{ MHz}$ . Table 2 lists the frequency ranges for each spw.

We use CASA (McMullin et al. 2007) for standard calibration and imaging of the continuum and spectral lines with `tclean`. Because of the rich spectra, we manually flag the lines for the continuum imaging. The spectra of spw10 and spw11 are combined for the imaging because the broad SiO emission. The spectra is cleaned down to 0.022 Jy, except for the spw04, which is cleaned down to 0.008 Jy due to its lower spectral resolution. The line imaging used the “multiscale” deconvolver with a robust parameter of 0.5, because the targeted emission traces different spatial scales (e.g. SiO for outflows and COMs for the inner envelope/disk).

The synthesized beam is about  $0''.6 \times 0''.4$  (Table 3). The Perseus molecular cloud is not at a single distance. Many studies assume a distance of 235 pc for Perseus based on the maser observations toward NGC 1333 SVS 13 (Hirota et al. 2008). Recently, Ortiz-León et al. (2018) derive a distance of  $321 \pm 10 \text{ pc}$  for IC 348 using VLBA and a distance of  $293 \pm 22 \text{ pc}$  for NGC 1333 using *Gaia* parallaxes. Zucker et al. (2020) combine the *Gaia* parallaxes and photometric data with a Bayesian framework to revise the distances toward different sightlines of Perseus, resulting in distances ranging from 234 pc to 331 pc. In this study, we assume a distance of 300 pc for the entire Perseus cloud. Thus, the synthesized beam is about  $180 \text{ au} \times 120 \text{ au}$ .

### 3. ANALYSES

#### 3.1. Identification of Young Stellar Object

In the 37 field of view, 51 continuum peaks are identified. We use the CASA task `imfit` to iteratively fit for continuum sources down to  $5\sigma$  of the residual image within the central 70% of the primary beam size ( $20''$ ). For the field centered on Per-emb 16, the fitting uses a threshold of  $4\sigma$  and extends the mask to the entire primary beam as a continuum source, Per-emb 28, is detected toward the edge of the primary beam where the noise is elevated. The continuum of the multiple systems are manually fitted to the individual continuum peak. Two protostars, L1448 IRS 2E and SVS 3, become non-detection in our observations due to their low brightness. SVS 13C locates at the edge of the primary

beam, resulting in a noisy continuum. Thus, we exclude SVS 13C from this study, making a total of 50 protostars. **L1448 IRS 2E has CS emission.**

Figure 1 shows the continuum emission along with the fitted shapes, while Table 3 lists the properties of the continuum sources. The continuum emission peak appears as a compact circular or elliptical shape. Some sources show extended continuum emission resembling the shape of outflow cavities, such as Per-emb 22 A and B. Three sources, EDJ2009-237, Per-emb 60, and EDJ2009-172, show no spectral line and no reliable measurement of source velocity in literature; therefore, we exclude them from spectral extraction as well as the line identification and modeling. However, these three sources still contribute to the total number of sources for calculating the detection statistics.

The observations resolve or marginally resolve 90% (45 of 50) of the continuum sources. Our sample includes single sources as well as resolved and unresolved multiple systems. According to the VANDAM survey (Tobin et al. 2016), our sample contains eleven binary systems and one triple system. Two of eleven binary systems are resolved and the triple system appears as a single source and an unresolved binary. In total, 20% of the sources are unresolved binary.

Tychoniec et al. (2020) derive the central dust mass of Perseus protostars using the 9 mm VLA observations (VANDAM; see Table 3). Dust emission from the center of a protostar may be marginally optically thick at millimeter wavelengths (Ko et al. 2020), making the derived dust mass lower limits. Seven sources in our sample have the averaged continuum brightness temperature exceeding 10 K (Table 3). NGC 1333 IRAS 4A1 has a  $T_b$  of 21.9 K, the brightest among our sample. In fact, continuum opacity limits the detectability of COMs toward 4A1, where COMs appear as absorption at ALMA Band 7 (Sahu et al. 2019) and emission at centimeter wavelengths (De Simone et al. 2020). Toward the other six sources, Per-emb 33 A, NGC 1333 IRAS 4A2, NGC 1333 IRAS 4B1, Per-emb 5, B1-b S, and Per-emb 11 A, our observations detect several molecular lines from the central region, suggesting that the continuum opacity has less impact compared to that for IRAS 4A1. Previous observations also suggest less impact from the continuum opacity for NGC 1333 IRAS 4B1 (Belloche et al. 2020) and B1-b S (Marcelino et al. 2018). Most of the sources show averaged brightness temperatures lower than 10 K, suggesting that the continuum sources remain unresolved and have a negligible effect to the COMs emission. We take the  $T_b$  as a tracer of the averaged dust column densities. Constraining the actual column densities requires higher resolution observations.

**Table 1.** ALMA Projects for PEACHES

Project code	Observation time	Amplitude calibrator	Bandpass calibrator	Phase calibrator
2016.1.01501.S	2016-11-16, 19, 26, 29, 30	J0238+1636	J0237+2848	J0336+3218
2017.1.01462.S	2018-09-10, 12	J0237+2848	J0237+2848	J0336+3218

**Table 2.** Frequency Setup

Spectral window	2016.1.01501.S		2017.1.01462.S	
	frequency range	channel width	frequency range	channel width
spw00	243.483–243.542 GHz	122.070 kHz	243.502–243.561 GHz	122.070 kHz
spw01	243.878–243.937 GHz	122.070 kHz	243.897–243.956 GHz	122.070 kHz
spw02	244.200–244.259 GHz	122.070 kHz	244.219–244.278 GHz	122.070 kHz
spw03	244.898–244.957 GHz	122.070 kHz	244.917–244.975 GHz	122.070 kHz
spw04	246.186–247.124 GHz	976.562 kHz	245.805–246.743 GHz	976.562 kHz
spw05	257.489–257.548 GHz	122.070 kHz	257.509–257.568 GHz	122.070 kHz
spw06	258.218–258.276 GHz	122.070 kHz	258.238–258.296 GHz	122.070 kHz
spw07	259.288–259.347 GHz	122.070 kHz	259.308–259.366 GHz	122.070 kHz
spw08	258.974–259.032 GHz	122.070 kHz	258.993–259.052 GHz	122.070 kHz
spw09	262.046–262.104 GHz	122.070 kHz	262.066–262.124 GHz	122.070 kHz
spw10_spw11 <sup>a</sup>	260.442–260.551 GHz	122.070 kHz	260.462–260.571 GHz	122.070 kHz
spw12	261.787–261.845 GHz	122.070 kHz	261.807–261.865 GHz	122.070 kHz

<sup>a</sup> The spectra of spw10 and spw11 are combined to measure the baseline due to the broad SiO emission.

### 3.2. Spectral Extraction

The ALMA image cubes are post-processed to extract 1D spectra for identifying the emission of complex molecules and further analyses. COMs typically desorb from dust grains at  $T \gtrsim 100$  K, which coincidentally corresponds to  $\sim 100$  au for typical embedded protostars (e.g., Yang et al. 2020). Given the spatial resolution of  $\sim 0''.5$  ( $\sim 150$  au), we focus on the spectra toward the continuum sources to search for the COMs in the inner envelope. In most of the cases, COMs emission concentrates around the protostars at  $\lesssim 300$  au scale. Figure 2 shows representative sample of the COMs emission, while the maps for the entire sample are shown in Appendix C. Three steps of post-processing reduces the image cubes to 1D spectra, which are summarized below.

- Extracting spectra: We use the CASA task `specflux` to extract the mean flux density within the ellipse which has the same major and minor axes as well as the position angle as the fitted continuum sources.
- Baseline calibration: The continuum has been removed before the imaging process; however, the extracted spectra sometimes still show imperfect baselines due to rich emission lines, lack of emission, and broad features. Thus, we manually se-

lect the frequency ranges for baseline calibration for each spectral window and each field.

- Velocity correction: Finally, the frequency of the extracted spectra are corrected according to the source velocities. We collect the source velocities from the literature as well as from the strong emission lines in our spectra, such as SO and CS. Table 3 lists the adopted source velocities and the corresponding references.

### 3.3. Line Identification and Modeling

Line identification starts with manual identification and verification for a few sources with rich spectra, including Per-emb-12B and B1-bS. We use SPLATALOGUE<sup>1</sup> to identify the molecular species and use XCLASS (Möller et al. 2017) to verify the identification. The XCLASS package is a LTE radiative transfer code that uses the molecular data from the Cologne Database of Molecular Spectroscopy (CDMS; Müller et al. 2001, 2005; Endres et al. 2016) and the Jet Propulsion Laboratory (JPL; Pickett et al. 1998). An identification needs to satisfy the following criteria.

<sup>1</sup> <http://www.splatalogue.net/>

**Table 3.** PEACHES Sample

Source	Common names	R.A. (J2000)	Decl. (J2000)	$v_{\text{lsr}}$	Ref. ( $v_{\text{lsr}}$ )	Beam	Cont. Size	$T_{\text{cont}}$	$M_{\text{dust}}^{\text{a}}$
		(hh:mm:ss)	(dd:mm:ss)	(km s $^{-1}$ )	( $\text{''}$ )	( $\text{''}$ )	(K)	(M $_{\oplus}$ )	
Per-emb 22 B		03:25:22.35	30:45:13.11	4.3	S19	0''64×0''39	0''95×0''51	0.92	23.1±13.0
Per-emb 22 A		03:25:22.41	30:45:13.26	4.3	S19	0''64×0''39	0''86×0''65	1.71	96.4±24.1
L1448 NW	L1448 IRS 3C	03:25:35.67	30:45:34.16	4.2	H18	0''64×0''39	0''83×0''47	3.15	382.4±54.9
Per-emb 33 B/C		03:25:36.32	30:45:15.19	5.3	S19	0''64×0''39	0''75×0''48	5.55	226.4±43.7
Per-emb 33 A		03:25:36.38	30:45:14.72	5.3	S19	0''64×0''39	0''73×0''45	10.33	294.0±57.6
L1448 IRS 3A		03:25:36.50	30:45:21.90	4.6	H18	0''64×0''39	0''85×0''59	3.21	235.1±47.8
Per-emb 26		03:25:38.88	30:44:05.28	5.4	S19	0''64×0''39	0''69×0''45	8.03	636.1±102.5
Per-emb 42		03:25:39.14	30:43:57.90	5.8	S19	0''64×0''39	0''64×0''39	0.66	116.5±29.0
Per-emb 25	IRAS 03235+3004	03:26:37.51	30:15:27.81	5.5	S18	0''64×0''39	0''69×0''41	5.27	172.6±65.4
Per-emb 17	L1455 IRS 1, IRAS 03245+3002	03:27:39.11	30:13:02.96	6.0	S19	0''64×0''40	0''79×0''48	2.00	199.4±34.0
Per-emb 20	L1455 IRS 4	03:27:43.28	30:12:28.88	5.3	S19	0''64×0''40	1''29×0''78	0.14	<31.1±15.5
L1455 IRS 2		03:27:47.69	30:12:04.33	5.1	H18	0''64×0''40	0''60×0''38	0.13	23.3±13.3
Per-emb 35 A	NGC 1333 IRAS 1	03:28:37.10	31:13:30.77	7.4	Y20	0''66×0''42	0''75×0''51	0.93	47.0±15.7
Per-emb 35 B	NGC 1333 IRAS 1	03:28:37.22	31:13:31.74	7.3	Y20	0''66×0''42	0''78×0''53	0.75	86.8±20.6
Per-emb 27	NGC 1333 IRAS 2A	03:28:55.57	31:14:36.97	6.5	Y20	0''66×0''42	0''93×0''66	5.79	683.7±93.6
EDJ2009-172		03:28:56.65	31:18:35.43	...	...	0''66×0''42	0''69×0''44	0.62	196.4±20.0
Per-emb 36	NGC 1333 IRAS 2B	03:28:57.37	31:14:15.77	6.9	S19	0''66×0''42	0''73×0''46	5.56	666.5±93.4
Per-emb 54	NGC 1333 IRAS 6	03:29:01.55	31:20:20.49	7.9	S19	0''66×0''42	0''69×0''40	0.07	115.5±28.2
SVS 13B	NGC 1333 SVS 13B	03:29:03.08	31:15:51.73	8.5	S19	0''66×0''42	0''87×0''68	6.64	581.1±98.2
SVS 13A2	VLA 3	03:29:03.39	31:16:01.58	8.4	S18	0''66×0''42	0''86×0''53	0.61	102.6±27.7
Per-emb 44	NGC 1333 SVS 13A	03:29:03.76	31:16:03.70	8.7	S19	0''66×0''42	0''98×0''79	6.84	674.4±90.9
Per-emb 15		03:29:04.06	31:14:46.23	6.8	S19	0''66×0''42	0''89×0''70	0.17	<9.3±6.6
Per-emb 50	IRAS 03260+3111 A	03:29:07.77	31:21:57.11	9.3	Y20	0''66×0''42	0''73×0''44	4.13	535.2±91.0
Per-emb 12 B	NGC 1333 IRAS 4A2	03:29:10.44	31:13:32.08	6.9	S19	0''66×0''42	1''33×0''81	10.04	158.1±38.4
Per-emb 12 A	NGC 1333 IRAS 4A1	03:29:10.54	31:13:30.93	6.9	S19	0''66×0''42	1''11×0''98	21.85	2853.9±437.0
Per-emb 21	NGC 1333 IRAS 7 SM2	03:29:10.67	31:18:20.16	8.6	Y20	0''66×0''42	0''74×0''48	2.05	211.9±41.1
Per-emb 18	NGC 1333 IRAS 7 SM1	03:29:11.27	31:18:31.09	8.1	S19	0''66×0''42	0''84×0''73	3.42	224.8±47.1
Per-emb 13	NGC 1333 IRAS 4B1	03:29:12.02	31:13:07.99	7.1	S19	0''66×0''42	1''07×0''83	14.76	1271.3±207.6
IRAS4B'	NGC 1333 IRAS 4B2	03:29:12.85	31:13:06.87	7.1	S19	0''66×0''42	0''83×0''74	7.13	603.2±115.2
Per-emb 14	NGC 1333 IRAS 4C	03:29:13.55	31:13:58.12	7.9	S19	0''66×0''42	0''79×0''50	3.05	311.2±58.6
EDJ2009-235		03:29:18.26	31:23:19.73	7.7	Y20	0''67×0''42	0''66×0''44	0.26	16.6±10.0
EDJ2009-237		03:29:18.74	31:23:25.24	...	...	0''67×0''42	0''67×0''42	0.12	...
Per-emb 37		03:29:18.97	31:23:14.28	7.5	Y20	0''67×0''42	0''82×0''57	0.56	95.4±23.9
Per-emb 60		03:29:20.05	31:24:07.35	...	...	0''67×0''42	0''73×0''47	0.08	<13.3±8.1
Per-emb 5	IRAS 03282+3035	03:31:20.94	30:45:30.24	7.3	S19	0''45×0''30	0''56×0''41	15.29	502.3±86.3
Per-emb 2	IRAS 03292+3039	03:32:17.92	30:49:47.81	7.0	S19	0''45×0''30	1''35×0''97	7.41	927.4±175.6
Per-emb 10	B1-d	03:33:16.43	31:06:52.01	6.4	S19	0''46×0''30	0''49×0''32	1.82	143.4±30.7
Per-emb 40	B1-a	03:33:16.67	31:07:54.87	7.4	S19	0''46×0''30	0''47×0''32	1.44	72.9±18.0
Per-emb 29	B1-c	03:33:17.88	31:09:31.74	6.1	Y20	0''46×0''30	0''56×0''39	8.41	233.5±43.5
B1-b N		03:33:21.21	31:07:43.63	6.6	C16	0''46×0''30	0''56×0''47	7.67	483.8±85.1
B1-b S		03:33:21.36	31:07:26.34	6.6	C16	0''46×0''30	0''63×0''53	14.79	354.0±76.5
Per-emb 16		03:43:50.97	32:03:24.12	8.8	S19	0''50×0''32	0''61×0''52	0.35	<34.9±18.1
Per-emb 28		03:43:51.01	32:03:08.02	8.6	S19	0''50×0''32	0''56×0''32	1.52	23.5±16.6
Per-emb 1	HH 211 MMS	03:43:56.81	32:00:50.16	9.4	S19	0''49×0''32	0''68×0''48	4.57	279.6±50.0
Per-emb 11 B	IC 348 MMS	03:43:56.88	32:03:03.08	9.0	S19	0''50×0''33	0''92×0''69	0.40	21.7±14.9
Per-emb 11 A	IC 348 MMS	03:43:57.07	32:03:04.76	9.0	S19	0''50×0''33	0''61×0''48	10.47	413.5±73.1
Per-emb 11 C	IC 348 MMS	03:43:57.70	32:03:09.82	9.0	S19	0''50×0''33	1''10×0''86	0.34	30.5±15.4
Per-emb 55	IRAS 03415+3152	03:44:43.30	32:01:31.22	12.0	S19	0''50×0''32	0''49×0''33	0.32	56.1±12.9
Per-emb 8		03:44:43.98	32:01:35.19	11.0	S19	0''50×0''32	0''49×0''36	8.51	237.9±47.5
Per-emb 53	B5 IRS 1	03:47:41.59	32:51:43.62	10.2	Y20	0''51×0''33	0''58×0''42	1.55	56.6±22.6

**References**—C16=Carney et al. (2016); H18=Higuchi et al. (2018); S18=Stephens et al. (2018); S19=Stephens et al. (2019); Y20=this study.

<sup>a</sup>The dust mass is taken from Tychoniec et al. (2020).

**NOTE**—The dust masses for L1455 IRS 2, EDJ2009-235, EDJ2009-172 are taken from Tychoniec et al. (2018) by applying a gas-to-dust ratio of 100. The dust mass of unresolved multiple systems, such as L1448 NW, Per-emb 33 B/C, Per-emb 17, Per-emb 44, Per-emb 27, Per-emb 36, and Per-emb 55, are taken to be the total mass of multiple protostars. The dust mass of Per-emb 40 is assumed to be the dust mass of Per-emb 40 A as the dust mass of Per-emb 40 B is an upper limit.

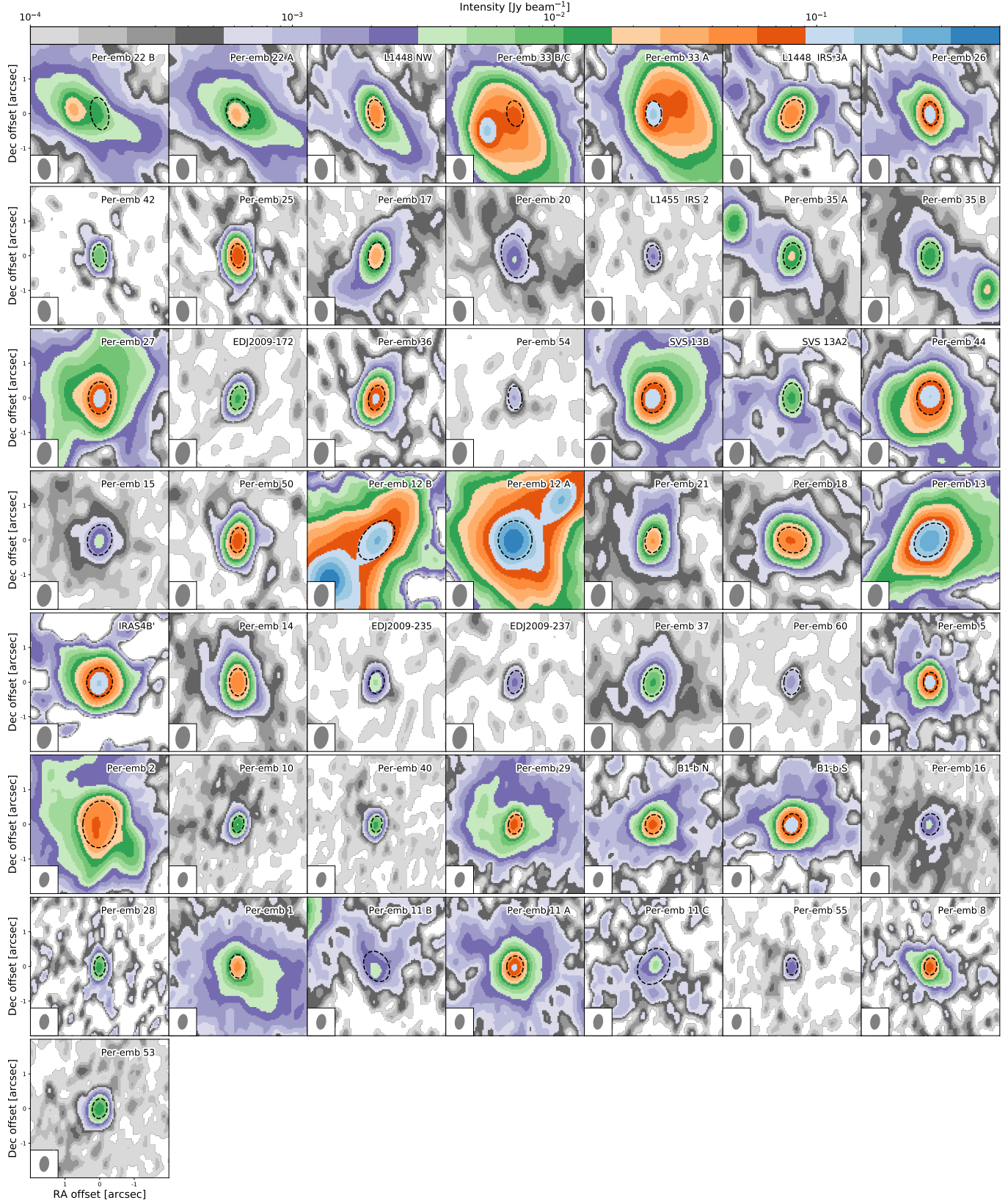


**Figure 1.** The continuum images of all PEACHES protostars. Non-detections toward L1448 IRS 2E and NGC 1333 SVS 3 are not shown. The dashed ellipses illustrate the size of fitted continuum, which is the region for extracting 1D spectra.

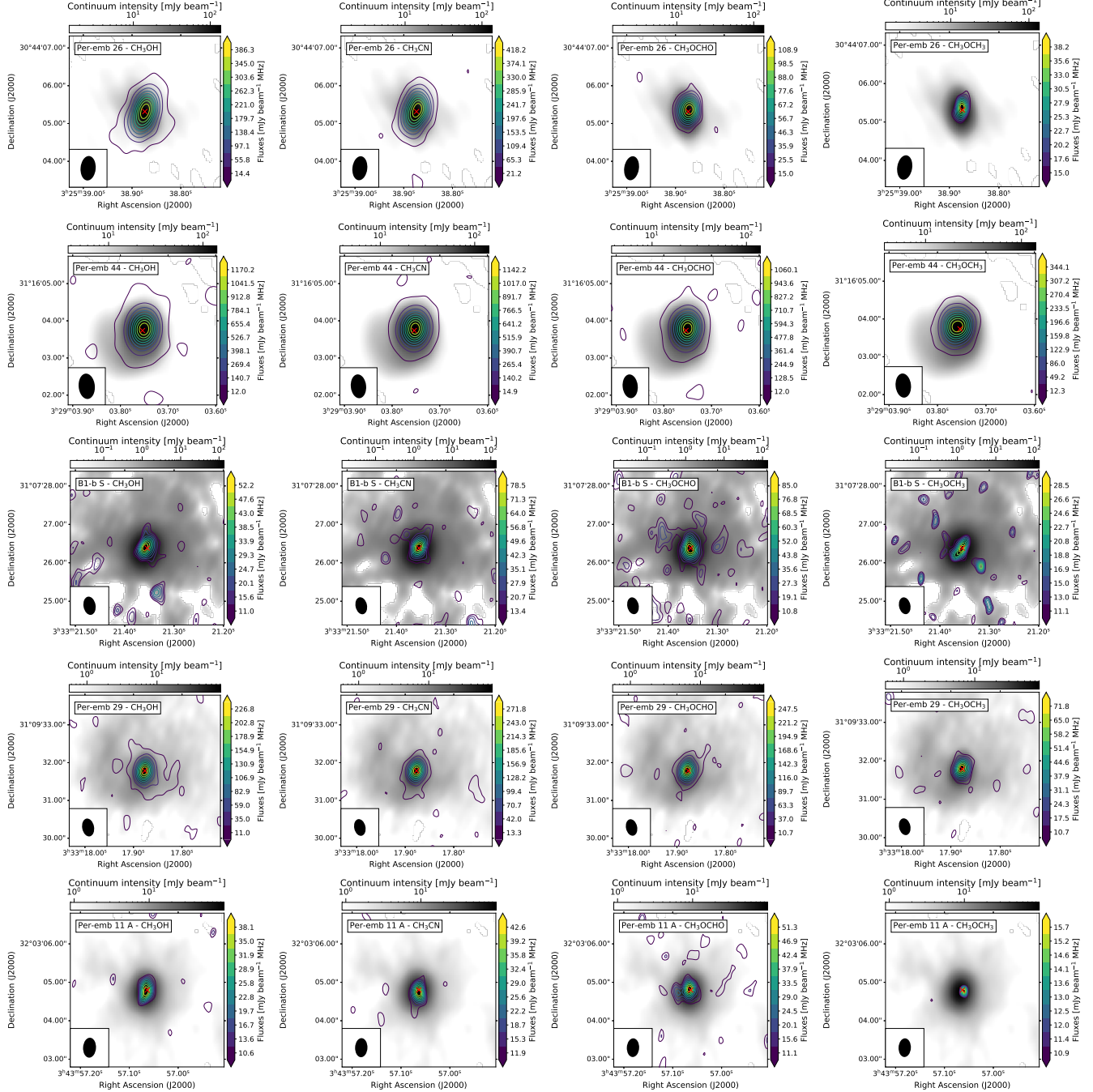


**Figure 2.** The intensity maps of most detected COMs, CH<sub>3</sub>OH, CH<sub>3</sub>CN, HCOOCH<sub>3</sub>, and CH<sub>3</sub>OCH<sub>3</sub> (from left to right). Each row shows the emission from Per-emb 26, Per-emb 44, B1-b S, B1-c, and Per-emb 11 A (top to bottom). The intensity is calculated by integrating over 3 km s<sup>-1</sup> around the line centroid, while the lowest contour shows the 3σ value. The grayscale images illustrate the continuum emission.

- The spectra agree with the predicted strengths of the model.
- The spectral lines are not all blended with other emission, such as other molecules and the SiO emission tracing the outflows. The emission of a few species, such as HDCO &  $^{13}\text{CH}_3\text{OH}$ ,  $\text{CH}_3\text{OH}$  &  $\text{HCOOCH}_3$ ,  $\text{CH}_3\text{CHO}$  &  $\text{CH}_2\text{DOH}$ ,  $^{34}\text{SO}$  &  $\text{C}_2\text{H}_5\text{OH}$ , and  $\text{CH}_3\text{OCH}_3$  &  $\text{CH}_2\text{DCN}$ , are partially blended (blending occurs at a few lines but other lines remain isolated). The fittings of those species are performed together to verify their identification.
- Identified molecules need to be already found toward young stellar objects as summarized in McGuire (2018).

Table 6 lists the identified species and transitions that are detected in at least one of the PEACHES protostars. Only identifiable transitions are listed. The xCLASS modeling include all the transitions in our frequency coverage for each molecule regardless their Einstein-A values and upper energy levels.

As shown in Figure 2, COMs emission centers around the protostars at  $\sim 100 - 200$  au. At the similar region, the gas density is around  $\sim 10^8 \text{ cm}^{-3}$  (B1-b S: Gerin et al. 2017), similar to the critical density of the COM emission detected in our observations. For example, the  $\text{CH}_3\text{OH}$  line at 243915 MHz has a critical density of  $1.4 \times 10^8 \text{ cm}^{-3}$  (Schöier et al. 2005; Rabli & Flower 2010). Thus, the assumption of LTE holds for modeling the COM emission. **YLY: B1-b S is one of the most dense protostars. My guess is that the COMs is close to LTE but not in LTE. We also test the LTE assumption on CH<sub>3</sub>OH with the large velocity gradient (LVG) model using RADEX (reference). The column density difference is only X%.**

Systematic spectral fitting using xCLASS is applied to all sources using a list of species, compiled from the identifications. Appendix A lists the catalogs used in this study. The fitting function in xCLASS includes several optimization algorithms that can be used in series to reduce biases. We configure the algorithm chain that starts with the genetic algorithm followed by the Levenberg-Marquardt  $\chi^2$  minimization. The genetic algorithm searches the best-fitting parameters iteratively with generations that evolve like a natural selection, where the better fitting models get less modification over generations. We setup the genetic algorithm to search for the top two best-fitting models with 30 generations. Then, the Levenberg-Marquardt  $\chi^2$  minimization applies to the two best-fitting models for 20 iterations to find the best-fitting models. The genetic algorithm aims

to find local minimums and the Levenberg-Marquardt minimization further finds the best-fitting models in the local minimums. The two best-fitting models found by the genetic algorithm often very similar, suggesting that there is only one minimum. To address the rare cases of two separated local minimums, we pick the model with the lower  $\chi^2$  values from the two best-fitting models constrained by the Levenberg-Marquardt minimization.

There are five parameters in the xCLASS modeling, the size of the emitting molecule ( $r_{\text{COM}}$ ), the excitation temperature ( $T_{\text{ex}}$ ), the column density ( $N_{\text{COM}}$ ), the line width ( $\Delta\nu$ ), and velocity offset ( $v_{\text{off}}$ ). We assume the COMs are all concentrated at the center, simplified as a 2D thin circular disk. We fix  $r_{\text{COM}}$  as  $0''.5$ , similar to our beam size, and optimize the model with five excitation temperatures, 100, 150, 200, 250, and 300 K. We allow the line width varying between  $1.2 \text{ km s}^{-1}$  to  $3.5 \text{ km s}^{-1}$  for better fitting quality but assume no velocity offset from the source velocity, and the allowed range of the column density for each molecule is chosen according to the strength of the emission. From the fitting results of five  $T_{\text{ex}}$ , if a molecule is detected, the mean column densities will be the best-fitting column density, while the range of the column densities indicates the upper and lower uncertainties. If a molecule is non-detection, the synthetic spectra for all lines are scaled to match the peaks of the each line fitted by a Gaussian profile. Then, we take the minimum of the corresponding column densities as the upper limit.

**YLY: The double-peaked line profile in Per-emb 17 has not properly modeled.**

## 4. RESULTS

### 4.1. Detection Statistics

We summarize the detection statistics in Figure 3, which includes COMs, the carbon-chain molecules, and the simple organic molecules, such as CS,  $\text{H}^{13}\text{CN}$ , SO,  $^{34}\text{SO}$ , and  $\text{SO}_2$ . In the following results of detection fraction, we include the three sources that are excluded from modeling due to no reliable source velocity, making a total of 50 sources. The COMs discussed here are the derived from the spectra taken toward the continuum peak (Section 3.1). We focus on the chemistry of COMs in the disk-forming regions in this study, therefore, excluding detection of molecules outside the continuum peak. A comparison of chemical composition in protostellar envelopes (100–1000 au) requires observations with larger maximum recoverable scale ( $\theta_{\text{MRS}}$ ).

The PEACHES protostars show a great chemical diversity from no molecule detected (e.g., B1-b N and L1455 IRS 2) to rich spectra of COMs (e.g., Per-emb 13). Most of the PEACHES protostars have simple or-

ganics, such as SO, CS, H<sup>13</sup>CN, and HDCO, and  $\sim 60\%$  of sources have SO<sub>2</sub> and <sup>34</sup>SO. Emission of C<sub>2</sub>H can be easily identified from the spectra. However, the C<sub>2</sub>H toward the continuum sources often shows irregular line profiles together with velocity offsets and absorption (Figure 17). In fact, warm environments, such as the outflow cavity wall, easily enhance the abundance of C<sub>2</sub>H because of elevated abundance of C<sup>+</sup> (e.g., Zhang et al. 2018; Imai et al. 2019). Thus, C<sub>2</sub>H emission is extended along with the outflow cavities, making the 1D spectra toward the continuum source unrepresentative. Observations with a larger  $\theta_{MRS}$  will provide a complete representation of the C<sub>2</sub>H abundance on the inner envelope.

Several sources have their SiO emission with a broad line width, significantly contaminating the emission of CH<sub>3</sub>CH<sub>2</sub>CN and CH<sub>3</sub>CHO. In the later quantitative discussion, we exclude the spectral windows contaminated by the SiO emission. For assigning the detections, we can distinguish the emission of CH<sub>3</sub>CH<sub>2</sub>CN and CH<sub>3</sub>CHO from the broad SiO emission in a few sources, such as CH<sub>3</sub>CHO in Per-emb 26.

Figure 4 shows the number of COMs detected toward the PEACHES sample. Twenty-one (42%) sources have no COMs detected. CH<sub>3</sub>OH is detected in 28 sources (56%); HCOOCH<sub>3</sub> is detected in 15 sources (32%); and N-bearing COMs are detected in 20 sources (40%). Comparing to the COMs in the CALYPSO survey (Bel-loche et al. 2020), the fraction of sources that have methanol,  $\sim 50\%$ , is similar to that for the PEACHES protostars. Also, 30% of the CALYPSO sources have at least three COMs, while 28% of the PEACHES protostars have at least three COMs.

We compare the number of detected COMs with the bolometric luminosity ( $L_{bol}$ ), the bolometric temperature ( $T_{bol}$ ), and the dust mass estimated by Tychoniec et al. (2020) using observations at 9 mm ( $M_{central}$ ). The number of COMs shows no obvious trend with  $L_{bol}$ ,  $T_{bol}$ , and  $M_{central}$ . For  $L_{bol}$ , the sources with at least three COMs all have  $L_{bol} \gtrsim 3 M_{\odot}$ , except for B1-b S. However, the sources without any COMs also have a similar  $L_{bol}$ . If COMs mostly come from thermal desorption, the region with  $T > T_{desorption}$  may be smaller for the low luminosity sources, making the emission of COMs fainter and reducing our sensitivity to detect COMs. The COM-rich sources have  $T_{bol} \sim 50$  K, while the COM-poor sources have a greater scatter of  $T_{bol}$ , ranging from 14.7 K to 1100 K. The protostars with high  $M_{central}$  ( $> 666.5 M_{\oplus}$ ) have detections of COMs. However, the protostars with low  $M_{central}$  can have either many COMs or no COM.

The sources with high continuum brightness temperature ( $T_{b,cont}$ ) tend to have rich spectra COMs (Figure 5), while the sources with no detection of COM have their  $T_{b,cont} \lesssim 10$  K. The brightest source in continuum, Per-emb 12 A has many molecules detected in absorption due to the high continuum opacity blocking the emission of COMs (Sahu et al. 2019; De Simone et al. 2020). The continuum brightness temperature traces the gas column density, tracing the amount of embedding gas around the protostars. Thus, the tendency between many COMs and the high  $T_{b,cont}$  hints the scenarios where the denser envelope either increases the detectability of COMs or enhance the complexity of molecules.

Compact emission of COMs ( $\sim 100$ –300 au) suggests a warm temperature ( $\gtrsim 100$  K) of COMs for a typical low-mass protostars (e.g. Yang et al. 2017), consistent with an origin of thermal desorption at the inner envelope, so called hot corinos (Ceccarelli 2004). Only L1448 IRS 3A shows extended CH<sub>3</sub>OH emission, and B1-b N shows no CH<sub>3</sub>OH emission toward the continuum but peaks at  $\sim 1''$  away from the continuum, hinting the existence of CH<sub>3</sub>OH toward the continuum source blocked by opaque continuum (Marcelino et al. 2018). Excluding L1448 IRS 3A, 28 sources (56%) have hot corinos type chemistry. Many of hot corinos are previously known (reference?), while our survey detects COMs other than CH<sub>3</sub>OH toward Per-emb 35 A, Per-emb 35 B, Per-emb 11 A, Per-emb 11 C, and HH 211 MMS.

## 4.2. Column Densities

### 4.2.1. Excitation Temperatures

The PEACHES spectra cover four methanol lines, while the spectra of each source include three of them due to the frequency shift in the wide spectral window. The three methanol lines have upper energy ranging from  $\sim 50$  K to  $\sim 500$  K, which allows us to estimate the rotational temperature of methanol if all three lines are detected. To construct the methanol rotational diagram, we fit the methanol emission with a Gaussian profile and bootstrap the measurements for fitting the rotational temperature. Figure 6 shows the rotational diagram of Per-emb 22 B along with the sampled rotational temperature. The derived rotational temperature of methanol ranges from 120 K to 240 K with an exception of Per-emb 18, which has a rotational temperature of 395.7 K for methanol (Table 4).

**YLY: need to redo and fix the MCMC fitting. The fitting shown here is  $\sim 6$  months old and somewhat does not work now.** For the sources with significant emission of HCOOCH<sub>3</sub>, the column density and the excitation temperature of HCOOCH<sub>3</sub> can be constrained with

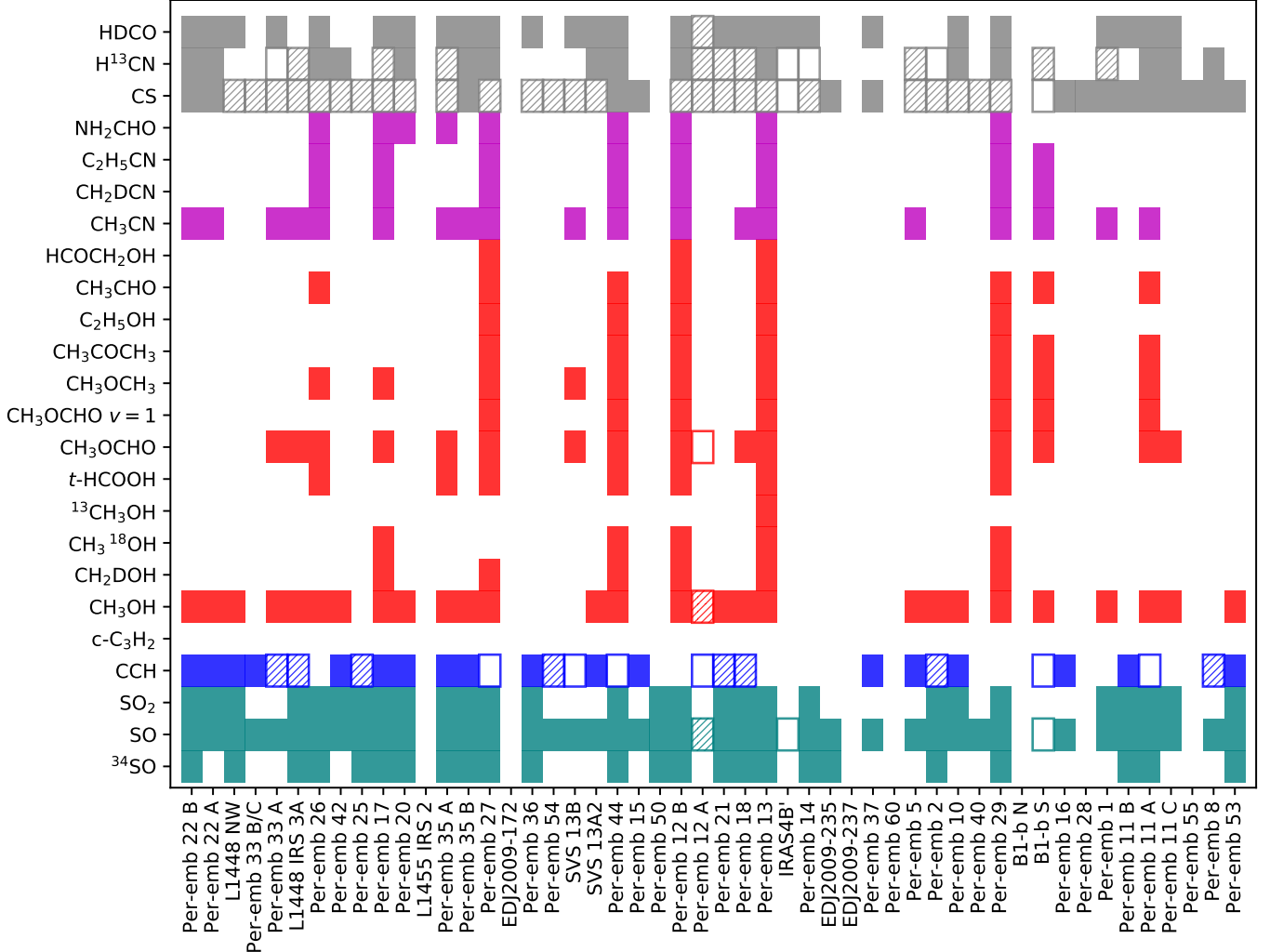


**Figure 3.** Summary of molecular detections. The sources are sorted by increasing R.A. from left to right. The detections are color-coded by the types of species: S-bearing molecules in green, carbon-chain molecules in blue, O-bearing COMs in red excluding N-bearing molecules, N-bearing COMs in magenta, other simple organics in gray. The boxes with solid colors indicate emission and the empty boxes indicate absorption. The hatched boxes indicate both emission and absorption are seen.

MCMC. Table 5 lists the sources where the MCMC fitting is feasible and the derived properties of  $\text{HCOOCH}_3$ . The best-fitting temperatures range from 100–300 K with a few outliers at  $\sim 1000$  K. The spectra with the high excitation temperature show non-Gaussian line profiles, making the fitting inaccurate. Therefore, we exclude those sources in Table 5.

#### 4.3. Correlations of COMs

The chemical evolution of protostars may leave certain patterns in the abundance of molecules as the dynamical evolution determines the density and temperature structures, which regulate chemical reactions. Thus, the abundance of COMs and their correlations provide critical information to constrain the chemical evolution at embedded protostars.

As described in Section 3.3, we fit the column density and line width with different excitation temperatures, resulting in a range of column density as its uncertainty. To quantify the goodness of correlation, we calculate the Pearson’s correlation coefficient ( $r$ ), which tests the linearity of two variables. A simple calculation of the Pearson’s correlation coefficient would ignore the uncertainties of the column density. Thus, we use the bootstrapping method to sample the fitted column densities to calculate Pearson’s  $r$ , by assuming a normal distribution centers on the best-fitted values with the uncertainty as the width of the normal distribution. If we include the upper limits as normal distributions center on zero, the correlation coefficient becomes significantly lower due to the cluster of samples around zero column density (Figure 8). With the detection-only sample, the

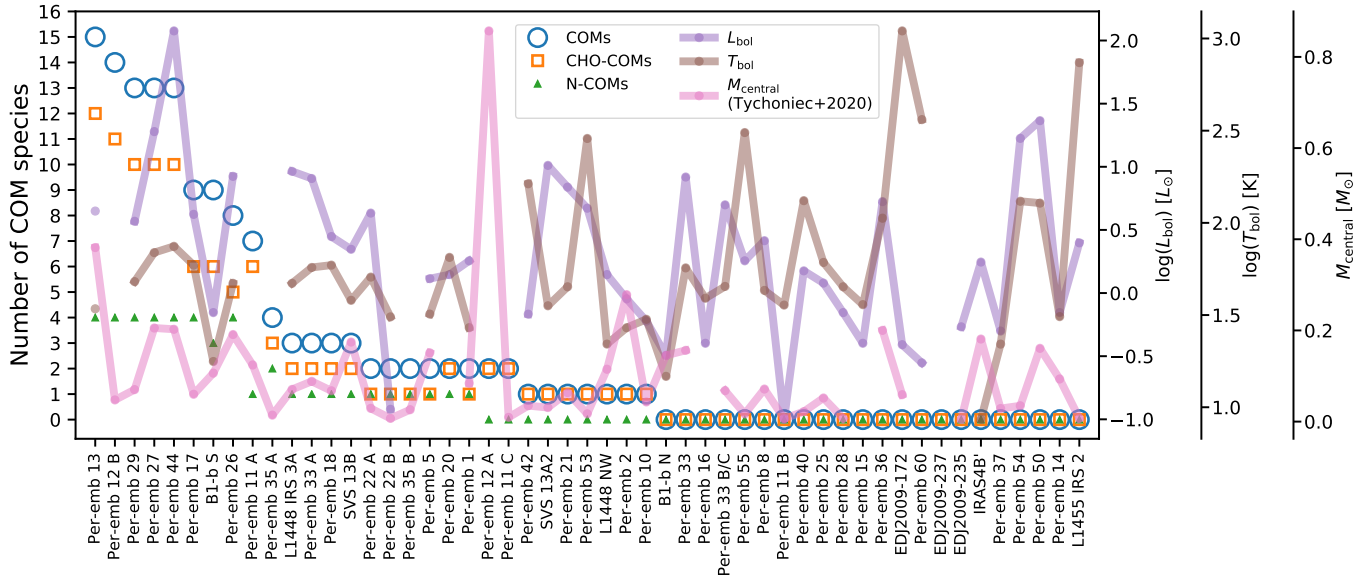


**Figure 4.** The number of COMs detected toward the PEACHES sources compared with the bolometric luminosity (purple), the bolometric temperature (brown), and the central dust mass (pink, Tychoniec et al. (2020)). The sources are sorted by the total number of COMs with the number of O-bearing COMs, N-bearing COMs, and all COMs labeled as orange boxes, green triangles, and blue circles, respectively. The mass of unresolved systems is estimated as the sum of each protostar. The bolometric luminosities and the bolometric temperatures are taken from Tobin et al. (2016) and Murillo et al. (2016).

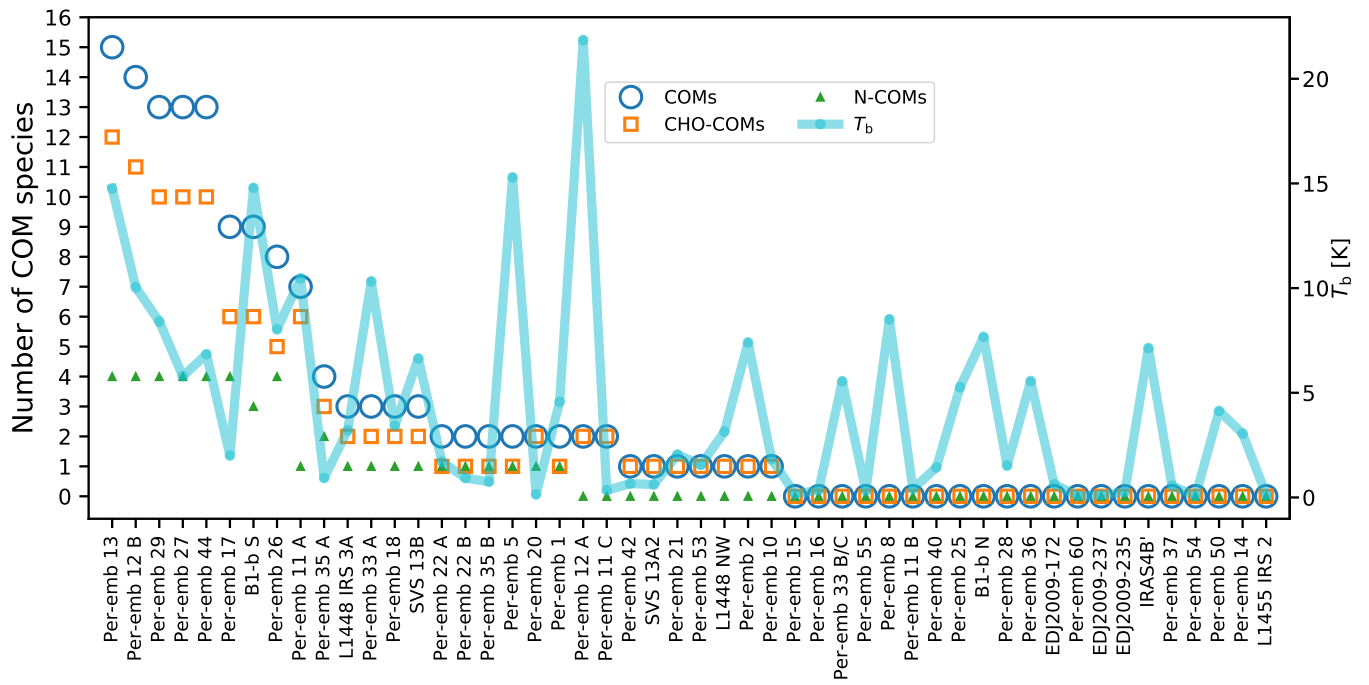


**Figure 5.** The number of COMs detected toward the PEACHES sources compared with the continuum brightness temperature. The legends for the protostars are the same as Figure 4. The brightness temperatures are indicated in green.

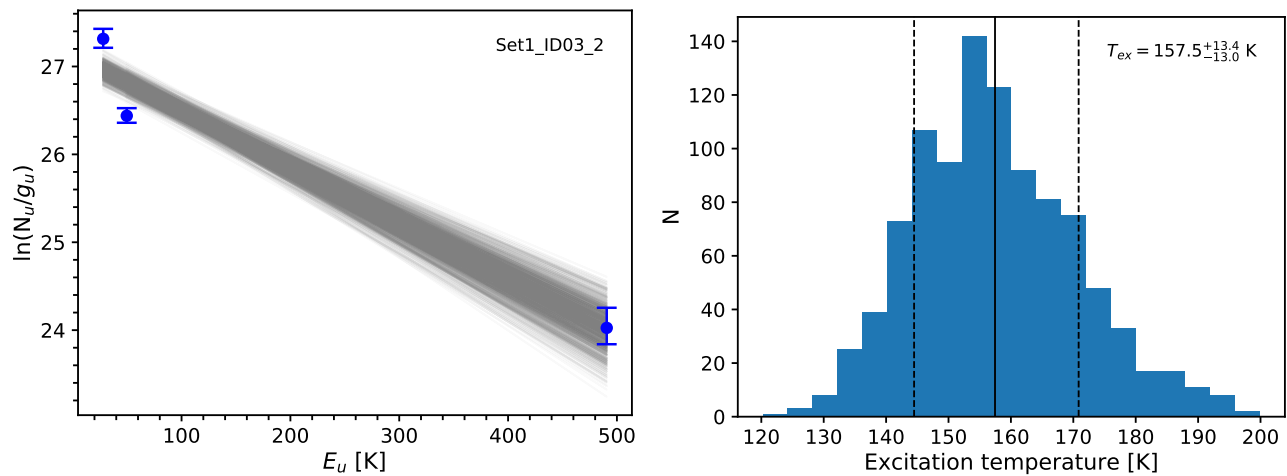


**Figure 6.** The methanol rotational diagram for Per-emb 22B and the fitted excitation temperature distribution using the bootstrapping method.

**Table 4.** Rotational Temperatures of Methanol

Source	$T_{\text{rot}}$
Per-emb 26	$120.1^{+2.6}_{-2.5}$ K
Per-emb 22 A	$182.4^{+11.2}_{-11.4}$ K
Per-emb 22 B	$157.5^{+13.4}_{-13.0}$ K
Per-emb 17	$173.9^{+1.8}_{-1.9}$ K
Per-emb 44	$197.5^{+0.3}_{-0.3}$ K
Per-emb 12 B	$194.0^{+0.8}_{-0.8}$ K
Per-emb 13	$208.6^{+3.9}_{-4.0}$ K
Per-emb 27	$195.8^{+0.4}_{-0.4}$ K
Per-emb 21	$151.0^{+14.6}_{-15.6}$ K
Per-emb 35 A	$145.1^{+3.7}_{-3.7}$ K
Per-emb 18	$395.7^{+30.7}_{-30.4}$ K
B1-bS	$241.7^{+11.7}_{-11.9}$ K
Per-emb 29	$227.7^{+3.2}_{-3.3}$ K

mean Pearson's  $r_d$  is 0.91, as expected for a tight correlation, with a Gaussian-like distribution skewed toward lower values. After including the upper limits, the mean Pearson's  $r$  decreases to 0.59 with larger uncertainty (the 68% credible interval increases by 160%). Thus, the bootstrapped correlation coefficient only considers the detections.

Figure 9 shows the correlations of several COMs selected from their detection rates as well as the ratios between species which is discussed in Section 5.2. The column density of CH<sub>3</sub>OH best correlates with that of CH<sub>3</sub>CN. Belloche et al. (2020) also found the tight correlation between these two molecules from the CALYPSO survey, which has a selective sample. The column densities of CH<sub>3</sub>OCH<sub>3</sub> and HCOOCH<sub>3</sub> also show a tight correlation. CH<sub>3</sub>OH also correlates with more complex species (i.e. so called daughter species, HCOOCH<sub>3</sub> and CH<sub>3</sub>OCH<sub>3</sub>) with a lower correlation coefficient than that between CH<sub>3</sub>OH and CH<sub>3</sub>CN. The correlations between CH<sub>3</sub>CN and more complex species also show the same behavior. The decreasing strength of correlation with between the simple COMs and more complex COMs supports the hypothesis that CH<sub>3</sub>OH and CH<sub>3</sub>CN are first generation species and HCOOCH<sub>3</sub> and CH<sub>3</sub>OCH<sub>3</sub> are the second generation (reference). The correlations of CH<sub>3</sub>OH, CH<sub>3</sub>CN, HCOOCH<sub>3</sub>, and CH<sub>3</sub>OCH<sub>3</sub> with other COMs show positive trends; however, the correlations are driven by a few sources due to the low detection rate of other COMs (Figure 11).

The column densities shown in Figure 9 and 11 are the column densities within a 0'5 region. The correlations remain similar for the column densities averaged within the extracted region. To directly compare the abundance of COMs, we normalize the column

densities of COMs by the  $T_{\text{b,cont}}$ , which is a proxy of gas column density. The normalized column densities of COMs show similar correlations as that of the column densities (Figure 10). We further normalize the "abundance" of COMs ( $N_{\text{COM}}/T_{\text{b}}$ ) with  $L_{\text{bol}}$  and  $T_{\text{bol}}$  to test the effect of the protostellar evolutionary stage on the observed complex chemistry (Figure 10, green and orange). After the normalization with  $L_{\text{bol}}$  and  $T_{\text{bol}}$ , the correlation coefficients remain similar for most cases. Normalized with  $L_{\text{bol}}$  and  $T_{\text{bol}}$ , the correlation between CH<sub>3</sub>OH and CH<sub>3</sub>OCH<sub>3</sub> decreases significantly, while CH<sub>3</sub>CN shows a moderate decrease of correlation with CH<sub>3</sub>OCH<sub>3</sub>. However, the correlations between HCOOCH<sub>3</sub> and CH<sub>3</sub>OCH<sub>3</sub> remain similar with different normalizations. The column densities correlations of CH<sub>3</sub>OH & CH<sub>3</sub>OCH<sub>3</sub> and CH<sub>3</sub>CN & CH<sub>3</sub>OCH<sub>3</sub> are also lower than that of other combinations of species. **Thus, the evolutionary stage of protostars plays an insignificant role on determining the abundance of most COMs but has a substantial effect for CH<sub>3</sub>OCH<sub>3</sub>.**

## 5. DISCUSSION

### 5.1. Universal Chemistry among Hot Corinos?

For the protostars with compact emission of COMs, so called hot corinos, the abundance of COMs correlates well between species. With the normalization of  $T_{\text{b,cont}}$ , the Pearson's  $r$  for the correlations between the four major species (CH<sub>3</sub>OH, CH<sub>3</sub>CN, HCOOCH<sub>3</sub>, and CH<sub>3</sub>OCH<sub>3</sub>) are 0.76–0.93 (Figure 10). The Pearson's  $r$  for the four major species with all COM species has a median value of 0.86 with a range from 0.57 to 0.95 (Figure 11). The correlations remain strong with the normalizations of  $L_{\text{bol}}$  and  $T_{\text{bol}}$ , suggesting that the chemistry of COMs may be independent of the evolutionary stage of protostars. The limited number of detections for the four major COMs with all COMs prohibits us to further quantify their correlation strengths.

We further test the effect of protostellar evolution with the abundance ratios of the four major COMs (Figure 12). The ratios of CH<sub>3</sub>CN/CH<sub>3</sub>OH and CH<sub>3</sub>OCH<sub>3</sub>/HCOOCH<sub>3</sub>, which are molecules with a similar complexity, have little variation as the functions of  $L_{\text{bol}}$ ,  $T_{\text{bol}}$ , and  $T_{\text{b,cont}}$ . In contrast, the ratios of HCOOCH<sub>3</sub> or CH<sub>3</sub>OCH<sub>3</sub> to CH<sub>3</sub>OH or CH<sub>3</sub>CN, which are the molecules with more complexity over the molecules with less complexity, increases with  $T_{\text{b,cont}}$ , whereas the ratios show tentatively decreases with  $L_{\text{bol}}$  and  $T_{\text{bol}}$ . Because of its high abundance, methanol may be more optical thick at a higher gas column density (high  $T_{\text{b,cont}}$ ), resulting in an underestimation of methanol column density, hence the elevated ratios. The emission of CH<sub>3</sub>CN is likely to be optical thin given

**Table 5.** MCMC Fitting of Methyl Formate

Source	Temperature [K]		$\log(\mathcal{N})$ [ $\text{cm}^{-2}$ ]		Line width [ $\text{km s}^{-1}$ ]	
	best	mode $\pm$ HPD	best	mode $\pm$ HPD	best	mode $\pm$ HPD
Set1_ID01_2	95	$76^{+315}_{-56}$	15.24	$15.29^{+0.42}_{-0.42}$	4.86	$4.77^{+0.22}_{-0.52}$
Set1_ID02	87	$98^{+14}_{-41}$	15.67	$15.67^{+0.10}_{-0.08}$	3.66	$4.06^{+0.65}_{-0.79}$
Set1_ID06	93	$93^{+59}_{-35}$	15.67	$15.67^{+0.12}_{-0.08}$	4.84	$4.77^{+0.22}_{-0.02}$
Set2_ID00	263	$310^{+3}_{-56}$	16.89	$16.92^{+0.05}_{-0.04}$	3.95	$3.95^{+0.15}_{-0.12}$
Set2_ID01_2	217	$194^{+75}_{-4}$	16.37	$16.36^{+0.10}_{-0.03}$	2.22	$2.25^{+0.14}_{-0.12}$
Set2_ID02	195	$225^{+119}_{-64}$	16.04	$16.10^{+0.20}_{-0.09}$	1.21	$1.21^{+0.00}_{-0.01}$
Set2_ID07	152	$131^{+281}_{-120}$	14.79	$14.72^{+0.53}_{-0.43}$	3.24	$1.66^{+2.26}_{-0.40}$
Set2_ID08	159	$10^{+551}_{-0}$	14.75	$14.11^{+0.85}_{-0.04}$	2.37	$1.20^{+2.15}_{-0.00}$
Set2_ID12	115	$41^{+269}_{-30}$	14.96	$15.02^{+0.05}_{-0.94}$	4.54	$4.89^{+0.09}_{-1.70}$
Set3_ID00	98	$58^{+41}_{-14}$	15.85	$15.82^{+0.26}_{-0.09}$	1.24	$1.25^{+0.02}_{-0.05}$
Set3_ID01	134	$134^{+13}_{-27}$	16.59	$16.60^{+0.02}_{-0.02}$	3.04	$3.08^{+0.18}_{-0.15}$
Set3_ID07	104	$92^{+182}_{-45}$	15.67	$15.67^{+0.29}_{-0.15}$	2.44	$2.33^{+1.22}_{-0.66}$

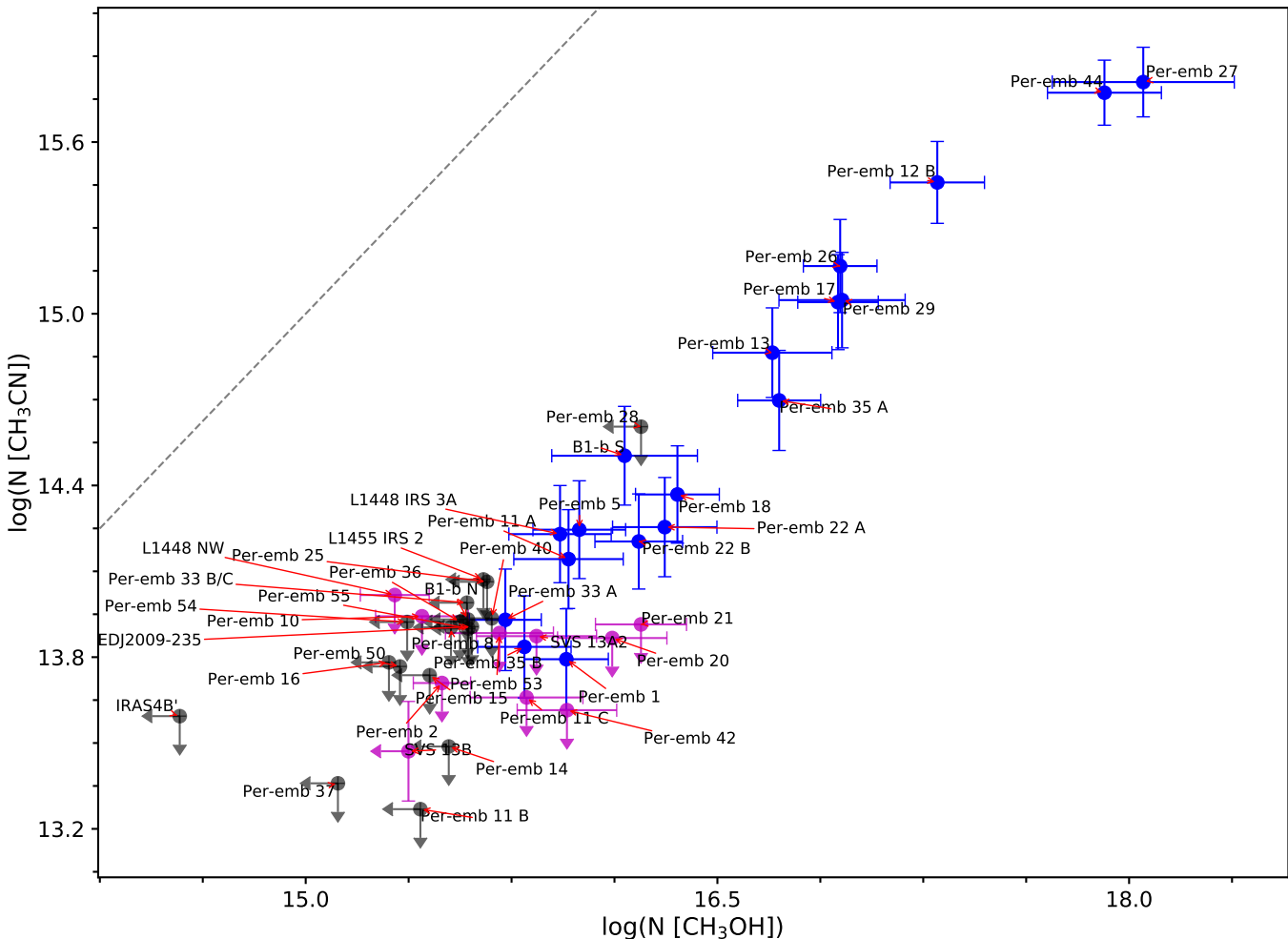


**Figure 7.** Correlation of the fitted column densities of  $\text{CH}_3\text{OH}$  and  $\text{CH}_3\text{CN}$  from the PEACHES protostars. The sources where both molecules are detected are shown in black; the sources where only one molecule is detected are shown in magenta; finally, the sources where both molecules are not detected are shown in black for the corresponding upper limits.

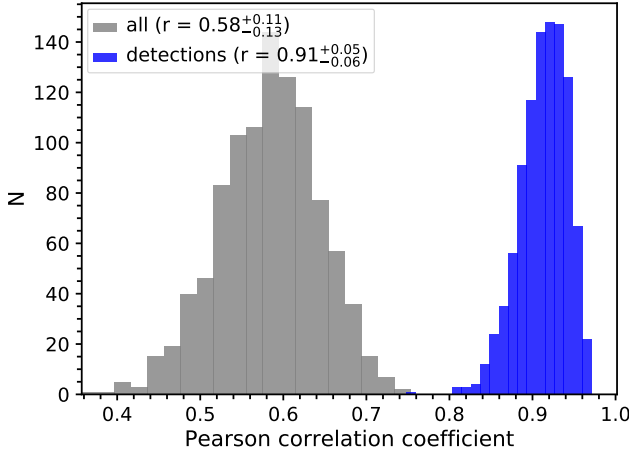


**Figure 8.** Distributions of Pearson’s correlation coefficient from 10000 resamples drawn from detections + non-detections and only detections. The legend indicates the mean values of Pearson’s  $r$  along with the range of the 95% credible interval as the associated uncertainties.

its low abundance compared to that of  $\text{CH}_3\text{OH}$ . Therefore, the insignificant trend in ratios of  $\text{CH}_3\text{CN}/\text{CH}_3\text{OH}$  with  $T_{\text{b},\text{cont}}$  indicates a negligible role of optical depth. Chemical evolution is an alternative scenario for such trend. Under the scheme of grain-surface chemistry,  $\text{CH}_3\text{OH}$  primarily forms from the hydrogenation of  $\text{CH}_3\text{O}$  or  $\text{CH}_2\text{OH}$ , while  $\text{HCOOCH}_3$  primarily forms from the reaction of  $\text{HCO}$  and  $\text{CH}_3\text{O}$  and  $\text{CH}_3\text{OCH}_3$  primarily forms from the reaction of  $\text{CH}_3$  and  $\text{CH}_3\text{O}$  (Garrod et al. 2008). Thus, the elevated ratios of  $\text{HCOOCH}_3$  and  $\text{CH}_3\text{OCH}_3$  to  $\text{CH}_3\text{OH}$  hint a higher abundance of  $\text{HCO}$  and  $\text{CH}_3$  at high  $T_{\text{b},\text{cont}}$  sources for more efficient formation of  $\text{HCOOCH}_3$ .

Higuchi et al. (2018) find a tentative trend that the sources closer to the edge of the cloud or the isolated sources show a higher ratio of  $\text{C}_2\text{H}$  to  $\text{CH}_3\text{OH}$ . With the spectra toward the continuum sources, we can test the correlation between the abundance of COMs and the location of the sources in the cloud. We follow the same approach described in Higuchi et al. (2018) to calculate the minimum distance from the source to the edge of the cloud that is arbitrarily defined as the  $10\sigma$  level in the Planck 217 GHz observations<sup>2</sup>. The minimum distance has no obvious effect to the normalized column density of  $\text{CH}_3\text{OH}$  (Figure 13). The abundance of  $\text{C}_2\text{H}$  may increase at small minimum distance, which requires

<sup>2</sup> Based on observations obtained with Planck (<http://www.esa.int/Planck>), an ESA science mission with instruments and contributions directly funded by ESA Member States, NASA, and Canada.

a comprehensive analysis of the  $\text{C}_2\text{H}$  emission to confirm that will be present in future papers.

YLY: should probably test size of COMs vs. Lbol

## 5.2. The Abundance Ratios of O-bearing and N-bearing COMs

The abundance ratios of COMs represent the chemistry of COMs. Figure 14 compares the abundance ratios of COMs toward the PEACHES protostars to the ratios from the CALYPSO survey (Belloche et al. 2020) and the observations of individual protostars as well as the model predictions from Garrod (2013). Belloche et al. (2020) divide up the CALYPSO sample into three groups, where Group 1 has low abundance of O-bearing COMs to  $\text{CH}_3\text{OH}$  and Group 3 has enhanced and reduced abundance relative  $\text{CH}_3\text{OH}$  for the cyanide and O-bearing COMs, respectively. The abundance ratios of COMs toward the PEACHES protostars generally agree with the ratios from the CALYPSO survey, which is expected due to the significant overlapped sample. Three of four sources in Group 2 are Perseus protostars. Interestingly, the ratios of COMs in the PEACHES protostars are significantly higher than that of well-known hot corinos, such as IRAS 16293–2422 B. Despite relative low ratios of COMs, the high column density of  $\text{CH}_3\text{OH}$ ,  $\gtrsim 10^{18} \text{ cm}^{-2}$  greatly increases the detectability of COMs toward these individual sources. The ratios of COMs toward the PEACHES protostars disagree with the peak abundance ratios in the warm-up models by Garrod (2013), where the models underestimate the abundance ratios for most of the O-bearing COMs except for  $\text{CH}_2\text{OHCHO}$  and are consistent with the ratios of N-bearing COMs.

Sakai : [please mention about abundance ratios  $\text{C}_2\text{H}_5\text{CN}$ ,  $\text{NH}_3\text{CHO}$  vs  $\text{CH}_3\text{OCH}_3$  and  $\text{CH}_3\text{OCHO}$ . and refer several papers discussed the O- and N difference. such as in Orion KL and/or IRAS16293??] O- and N-difference might be enhanced in more complex species (?).

## 5.3. Origin of the $\text{CH}_3\text{OH}/\text{CH}_3\text{CN}$ Correlation

The tight correlation between  $\text{CH}_3\text{OH}$  and  $\text{CH}_3\text{CN}$  is a striking finding of the PEACHES survey, while studies such as Bergner et al. (2017); Belloche et al. (2020) have shown a similar trend with fewer detections or larger scatter. Belloche et al. (2020) argue that this correlation between  $\text{CH}_3\text{OH}$  and  $\text{CH}_3\text{CN}$  may not be due to chemistry because of the somewhat unrelated formation pathways of two molecules. If the gas-phase chemistry is negligible for the production of  $\text{CH}_3\text{OH}$  and  $\text{CH}_3\text{CN}$ , the tight correlation between  $\text{CH}_3\text{OH}$  and  $\text{CH}_3\text{CN}$  suggests a similar abundance ratio of two molecules on the

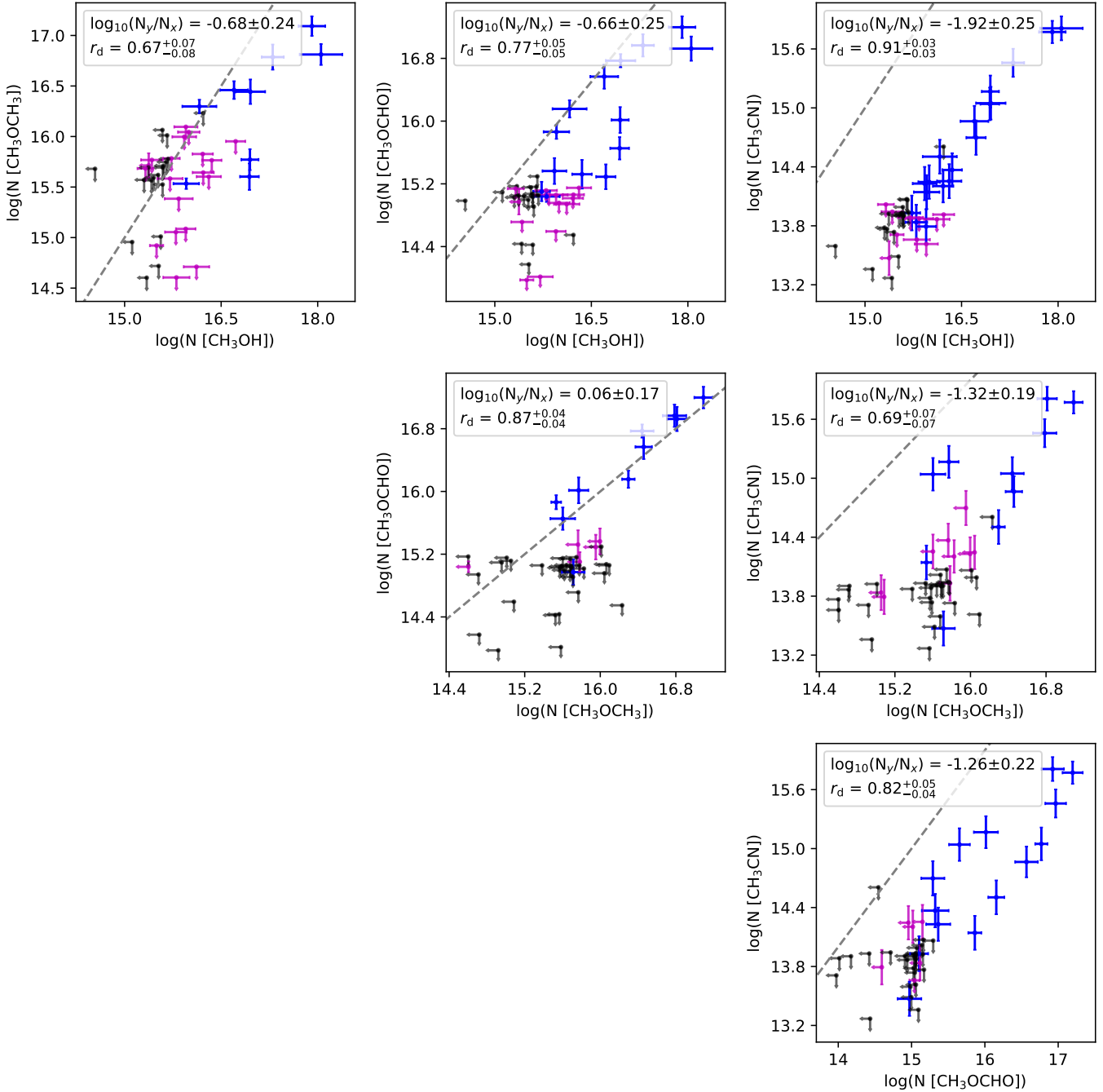


**Figure 9.** Corner plot of the correlations of the column densities between  $\text{CH}_3\text{OH}$ ,  $\text{CH}_3\text{CN}$ ,  $\text{HCOOCH}_3$ , and  $\text{CH}_3\text{OCHO}$ . The color code follows that in Figure 7. The dashed line indicates equality. The legends indicate the Pearson's  $r$  ( $r_d$ ) and the logarithmic ratio of the two molecules ( $N_y/N_x$ ) for the detection-only sample. The four most detected COMs are shown in this figure, while other COMs are shown in Figure 11.

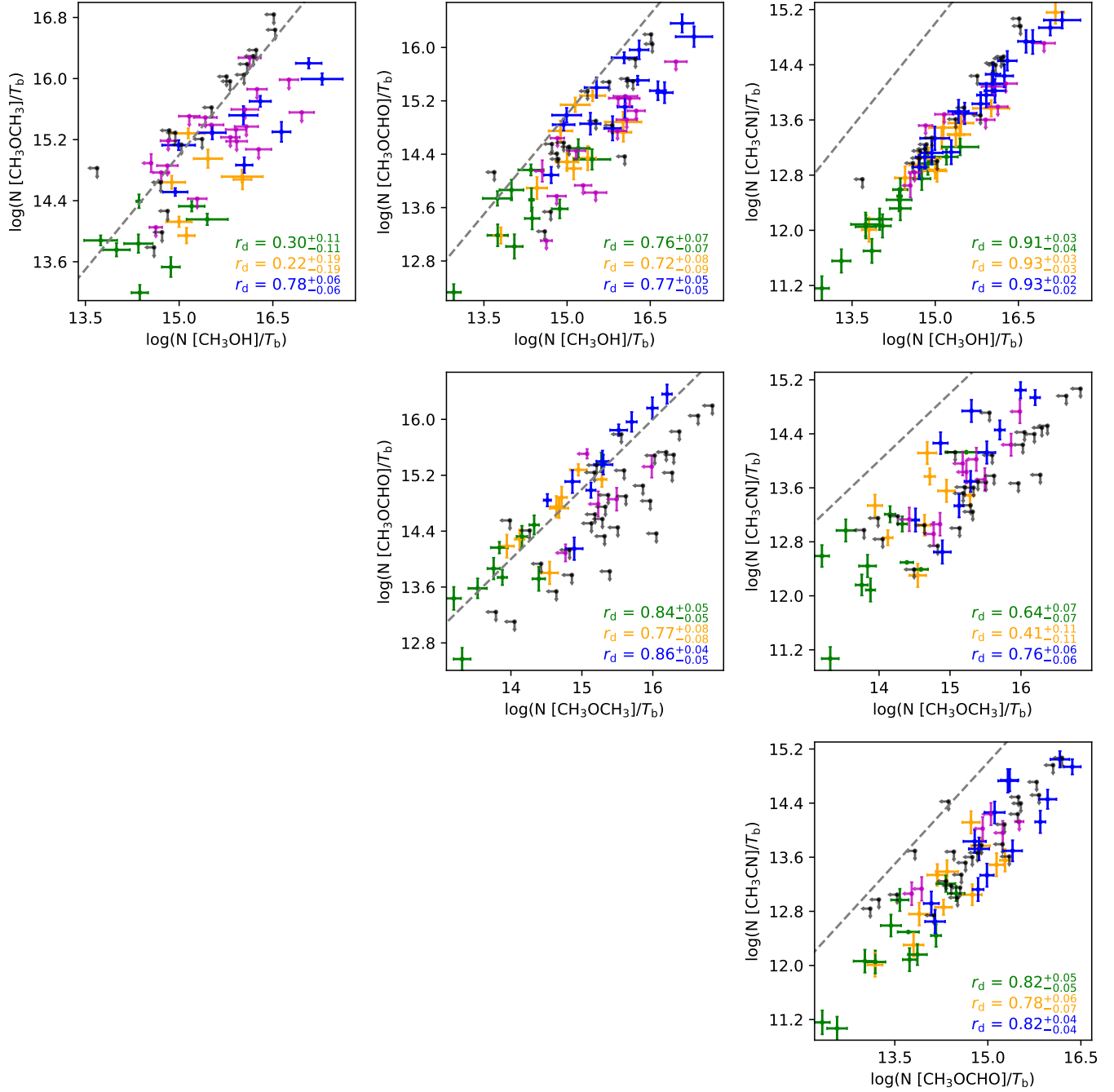


**Figure 10.** Corner plot of the correlations of the normalized column densities. The blue, magenta, and black symbols indicate the column densities normalized by the continuum brightness temperature ( $T_{\text{b},\text{cont}}$ ), while the color scheme follows that in Figure 7. The orange symbols show the column densities normalized by  $T_{\text{b},\text{cont}}$  and the bolometric luminosity ( $L_{\text{bol}}$ ), while the green symbols show that normalized by  $T_{\text{b},\text{cont}}$  and the bolometric temperature ( $T_{\text{bol}}$ ). We only show the column densities if both molecules are detected for the ones normalized by  $T_{\text{b},\text{cont}} T_{\text{bol}}$  and  $T_{\text{b},\text{cont}} L_{\text{bol}}$ . The Pearson's  $r$  correlation coefficient for the detections with each normalization is shown in the legend with corresponding color. A few close multiple sources, including Per-emb 12 A & B, Per-emb 35 A & B, and Per-emb 11 A & C, are excluded for the normalization of  $T_{\text{bol}}$  and  $L_{\text{bol}}$  due to their poorly determined SEDs.

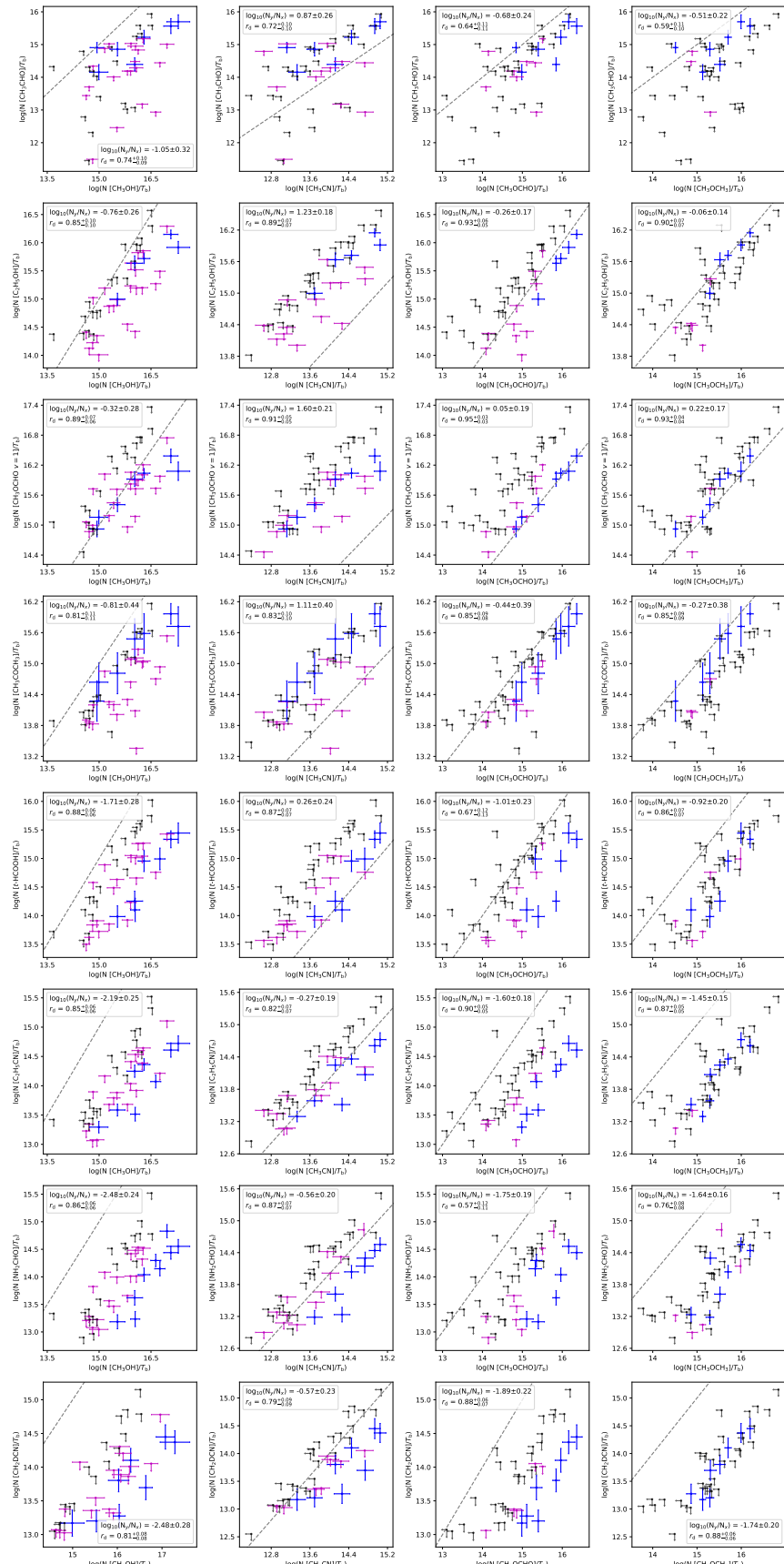


**Figure 11.** Corner plot of the correlations of the column densities normalized by the continuum brightness temperature between the more abundance COMs,  $\text{CH}_3\text{OH}$ ,  $\text{CH}_3\text{CN}$ ,  $\text{HCOOCH}_3$ , and  $\text{CH}_3\text{OCH}_3$ , and the less abundance COMs  $\text{CH}_3\text{CHO}$ ,  $\text{C}_2\text{H}_5\text{OH}$ ,  $\text{HCOOCH}_3$   $v = 1$ ,  $\text{CH}_3\text{COCH}_3$ ,  $\text{CH}_3\text{CH}_2\text{CN}$ ,  $t\text{-HCOOH}$ , and  $\text{NH}_2\text{CHO}$ . The legends are similar to Figure 7.

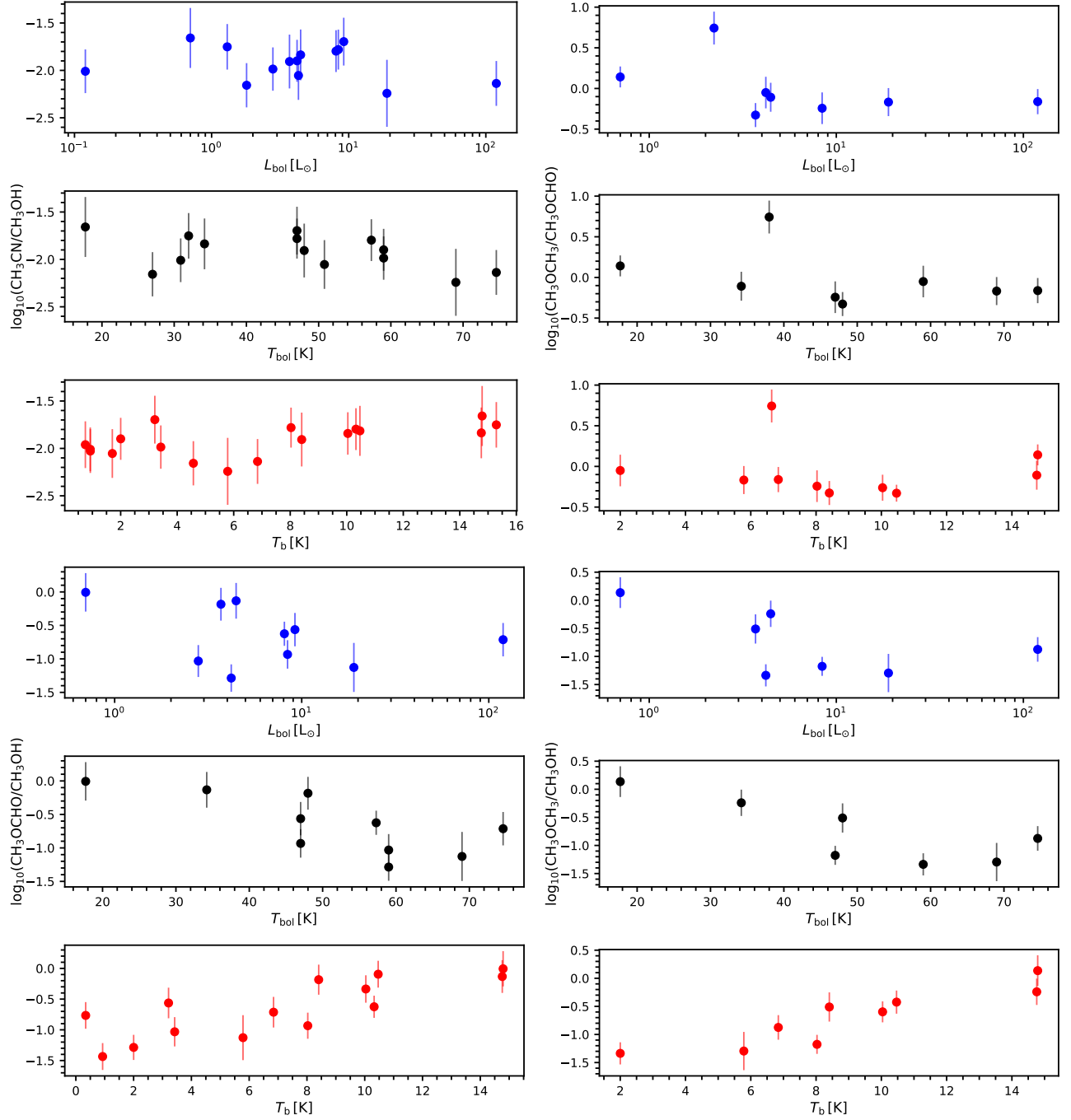


**Figure 12.** Ratios of well-detected molecules,  $\text{CH}_3\text{OH}$ ,  $\text{CH}_3\text{CN}$ ,  $\text{HCOOCH}_3$ , and  $\text{CH}_3\text{OCH}_3$ , as functions of  $L_{\text{bol}}$  (blue),  $T_{\text{bol}}$  (black), and  $T_b$  (red).

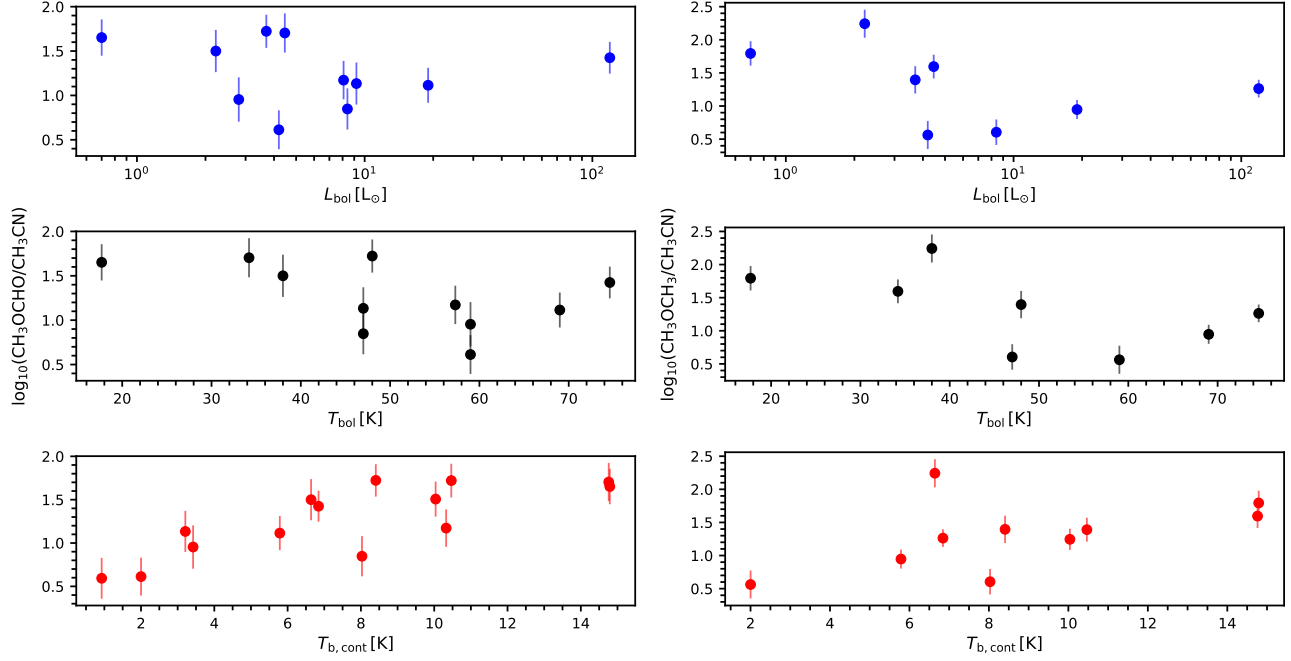
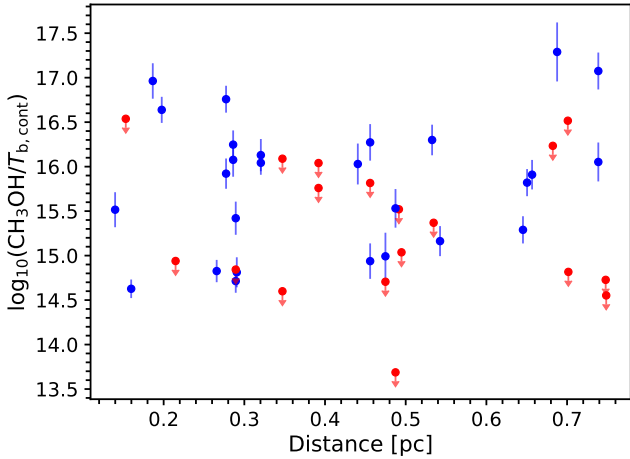


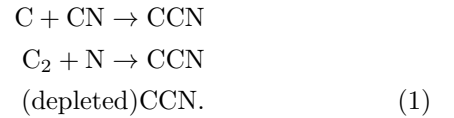
Figure 12 (Cont.).



**Figure 13.** The column densities of CH<sub>3</sub>OH toward the PEACHES protostars normalized by the averaged continuum brightness temperature as a function of the minimum distance to the 10 $\sigma$  contour in the Planck 217 GHz observations. Due to the lower brightness at 217 GHz toward Per-emb 5 and Per-emb 25, their minimum distances are calculated with 5 $\sigma$  and 3 $\sigma$  contours, respectively.

icy grains prior to being thermally desorbed. Thus, the chemical processes that produce these two molecules may occur at a much shorter timescale compared to the dynamical scale of the protostellar evolution, hinting a universal chemistry of COMs at the warm protostellar envelope. The tight correlation may also reflect a uniform elemental abundance of O and N in the Perseus molecular cloud before the star formation.

The compact emission of CH<sub>3</sub>OH has a well known icy origin, where CH<sub>3</sub>OH forms via the hydrogenation on the surface of dust grains. At cold temperature, the non-thermal desorption is thought to responsible for the production of CH<sub>3</sub>OH. CH<sub>3</sub>CN can also form in gas-phase via radiative association (HCN + CH<sub>3</sub><sup>+</sup>  $\rightarrow$  CH<sub>3</sub>CNH<sup>+</sup> +  $h\nu$ ) followed by the dissociative recombination of CH<sub>3</sub>CNH<sup>+</sup> or on the grain surface. The grain-surface reactions to form CH<sub>3</sub>CN can occur at cold temperature by the hydrogenation of CCN, which can form via



At warm temperature, CH<sub>3</sub>CN can form directly from reactions between radicals, CH<sub>3</sub> and CN. For embedded protostars, the grain-surface reactions are thought to dominate the production of CH<sub>3</sub>CN; however, it remains unclear whether the cold phase or warm phase grain-surface pathway regulates the abundance of CH<sub>3</sub>CN.

If we assume an icy grain origin for both CH<sub>3</sub>OH and CH<sub>3</sub>CN, we can test the efficiency of the cold and warm phase pathways by comparing the ratio of CH<sub>3</sub>CN/CH<sub>3</sub>OH toward the prestellar and protostellar sources. **YLY:** methanol must be released from dust grains via non-thermal reactions. I recall there are some chemical reactions that can form methanol other than the grain-surface chemistry, perhaps some form of gas-phase chemistry, but don't know for sure now. At

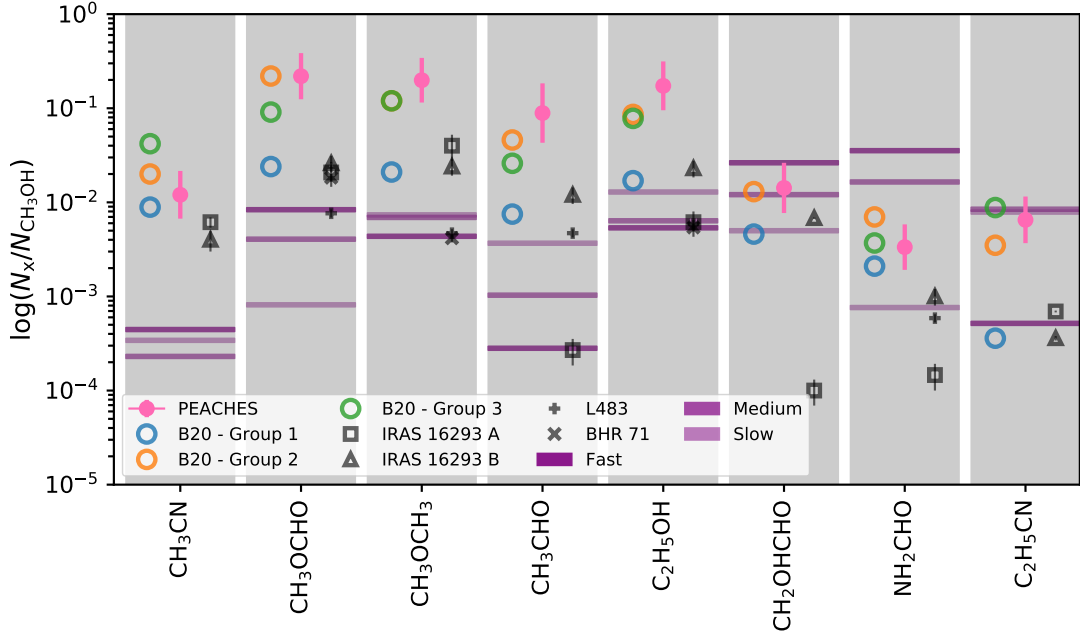


**Figure 14.** The ratios of the COMs commonly found in the PEACHES survey and the CALYPSO survey (Belloche et al. 2020) as well as a few selected hot corinos. The CALYPSO sources are categorized into three groups according to their COMs abundance to  $\text{CH}_3\text{OH}$ . Group 3 has no detection of  $\text{CH}_2\text{OHCHO}$ . The column densities of COMs toward IRAS 16293–2422 B are taken from Jørgensen et al. (2016) for  $\text{CH}_3\text{OH}$ , Jørgensen et al. (2018) for  $\text{C}_2\text{H}_5\text{OH}$ ,  $\text{CH}_3\text{OCH}_3$ ,  $\text{HCOOCH}_3$ ,  $\text{CH}_3\text{CHO}$ ,  $\text{NH}_2\text{CHO}$ , and  $\text{CH}_2\text{OHCHO}$ , Calcutt et al. (2018) for  $\text{CH}_3\text{CN}$  and  $\text{CH}_3\text{CH}_2\text{CN}$ . The column densities of COMs toward IRAS 16293–2422 A are taken from Manigand et al. (2020) for  $\text{CH}_3\text{OH}$ ,  $\text{C}_2\text{H}_5\text{OH}$ ,  $\text{CH}_3\text{OCH}_3$ ,  $\text{HCOOCH}_3$ ,  $\text{CH}_3\text{CHO}$ ,  $\text{NH}_2\text{CHO}$ , and  $\text{CH}_2\text{OHCHO}$ , Calcutt et al. (2018) for  $\text{CH}_3\text{CN}$  and  $\text{CH}_3\text{CH}_2\text{CN}$ . The column densities of COMs toward L483 are taken from Jacobsen et al. (2019). The column densities of COMs toward BHR 71 are taken from Yang et al. (2020), assuming a  $T_{\text{ex}}$  of 100 K for  $\text{CH}_3\text{OH}$ . The purple lines indicate the peak abundance ratios to  $\text{CH}_3\text{OH}$  from the warm-up model in Garrod (2013), where the “Fast”, “Medium”, and “Slow” represent the speed of the warm-up process plotted in different transparency.

prestellar cores,  $[\text{CH}_3\text{CN}/\text{CH}_3\text{OH}]$  are 0.28, 0.039, and 0.042 for TMC1 (Gratier et al. 2016), L1521 E (Nagy et al. 2019), and L1544 (Nagy et al. 2019), respectively, all of which are higher than the ratio in our survey,  $0.012^{+0.009}_{-0.005}$ . The decreases of  $[\text{CH}_3\text{CN}/\text{CH}_3\text{OH}]$  from prestellar to protostellar phase suggests that the warm phase grain-surface chemistry plays a rather insignificant role for the production of  $\text{CH}_3\text{CN}$  and/or the gas-phase chemistry is more efficient at the cold phase to produce additional  $\text{CH}_3\text{CN}$ .

## 6. CONCLUSIONS

This work presents the PEACHES survey, an unbiased chemistry survey of COMs toward 50 Class 0/I protostars at the Perseus molecular cloud using ALMA Band 6 observations. The main conclusions are:

1. Perseus Class 0/I protostars commonly (58%) show warm COMs emission.  $\text{CH}_3\text{OH}$  is the most detected species of COMs, while our observations show the emission of 12 O-bearing COMs and 4 N-bearing COMs, including isotopologues.
2. The good correlations between the most detect COMs,  $\text{CH}_3\text{OH}$ ,  $\text{CH}_3\text{CN}$ ,  $\text{HCOOCH}_3$ , and  $\text{CH}_3\text{OCH}_3$ , as well as between these COMs and other fewer detected COMs hint a universal chemistry of COMs for the Perseus embedded protostars. Protostellar properties, such as  $L_{\text{bol}}$ , the evolutionary indicator, such as  $T_{\text{bol}}$ , and the minimum distance to the cloud edge, have little impact to the number of detected COMs and the abundance of COMs.
3.  $\text{HCOOCH}_3$  and  $\text{CH}_3\text{OCH}_3$  are the most abundant COMs other than  $\text{CH}_3\text{OH}$  with abundance ratios to  $\text{CH}_3\text{OH}$  of  $0.22^{+0.17}_{-0.10}$  and  $0.21^{+0.15}_{-0.09}$ , respectively. The abundance of COMs to  $\text{CH}_3\text{OH}$  in the Perseus protostars are significantly higher than that of the well-known hot corinos, such as IRAS 16293–2422 B, and inconsistent with the model predictions by Garrod (2013).
4. A similar composition of  $\text{CH}_3\text{OH}$  and  $\text{CH}_3\text{CN}$  on the icy grains for the Perseus protostars may result in the observed extremely well correlated column densities of  $\text{CH}_3\text{OH}$  and  $\text{CH}_3\text{CN}$ .

5. The elevated abundance ratio of CH<sub>3</sub>CN to CH<sub>3</sub>OH at the prestellar phase indicates a more efficient gas-phase chemistry to produce CH<sub>3</sub>CN at the cold phase or an insignificant role of the warm-phase grain-surface chemistry for the abundance of CH<sub>3</sub>CN at the protostellar phase.
6. The ratios of more complex COMs, such as HCOOCH<sub>3</sub> and CH<sub>3</sub>OCH<sub>3</sub>, to the less complex COMs, such as CH<sub>3</sub>OH and CH<sub>3</sub>CN, increase as the averaged continuum brightness temperature, a proxy of the gas column density, suggesting an enhanced production of more complex COMs toward more embedded sources.

Y.-L. Yang acknowledges the supports from the JSPS Postdoctoral Fellowship from Japan Society

for the Promotion of Science and the Virginia Initiative of Cosmic Origins Postdoctoral Fellowship. This paper makes use of the following ALMA data: ADS/JAO.ALMA#2016.0.00391.S. ALMA is a partnership of ESO (representing its member states), NSF (USA) and NINS (Japan), together with NRC (Canada), MOST and ASIAA (Taiwan), and KASI (Republic of Korea), in cooperation with the Republic of Chile. The Joint ALMA Observatory is operated by ESO, AUI/NRAO and NAOJ. The National Radio Astronomy Observatory is a facility of the National Science Foundation operated under cooperative agreement by Associated Universities, Inc.

#### *Facilities:* ALMA

*Software:* astropy (Astropy Collaboration et al. 2018), XCLASS (Möller et al. 2017), spectral-cube (Robitaille et al. 2016), CASA (McMullin et al. 2007)

## APPENDIX

### A. CATALOGS FOR MOLECULAR DATA

The spectroscopic data are taken from the Cologne Database of Molecular Spectroscopy (CDMS; Müller et al. 2001, 2005; Endres et al. 2016) and the Jet Propulsion Laboratory (JPL; Pickett et al. 1998). Here we list only the references that cover the frequencies relevant to this study.

**YLY: to be updated. Maybe put into a table.** For CH<sub>3</sub>OH, the data were taken from Xu et al. (2008); for CH<sub>2</sub>DOH, the data were taken from Pearson et al. (2012); for <sup>13</sup>CH<sub>3</sub>OH, the data were taken from Xu & Lovas (1997). For HCOOCH<sub>3</sub>, the data were taken from Ilyushin et al. (2009), which includes the data from Plummer et al. (1984); Oesterling et al. (1999); Carvajal et al. (2007); Maeda et al. (2008). For CH<sub>3</sub>CHO, the data were taken from Kleiner et al. (1996). For CH<sub>3</sub>OCH<sub>3</sub>, the data were taken from Endres et al. (2009). For CH<sub>3</sub>COCH<sub>3</sub>, the data were taken from Groner et al. (2002). For CH<sub>3</sub>C<sup>15</sup>N, the data were taken from Müller et al. (2009) together with the data from Pearson & Mueller (1996). For gauche-C<sub>2</sub>H<sub>5</sub>OH, the data were taken from Pearson et al. (2008) together with the data from Pearson et al. (1996). For CH<sub>3</sub>CH<sub>2</sub>CN, the data were compiled from Pearson et al. (1994); Brauer et al. (2009). For SO<sub>2</sub>, the data were taken from Müller & Brünken (2005) with additional data from Lovas (1985); Helminger & De Lucia (1985); Belov et al. (1998).

### B. IDENTIFIED SPECIES AND TRANSITIONS

Table 6 lists the species and their transitions identified from the PEACHES spectra.

**Table 6.** Line Identification

Frequency (MHz)	Transition <sup>a</sup>	log(Einstein-A)	$E_u$ (K)	$g_u$	Ref.
Ethynyl (CCH)					
262065.00 (0.05)	[3, 5/2, 3]→[2, 3/2, 2] <sup>b</sup>	-4.31	25.16	7	CDMS
262067.47 (0.05)	[3, 5/2, 2]→[2, 3/2, 1] <sup>b</sup>	-4.35	25.16	5	CDMS
262078.93 (0.02)	[3, 5/2, 2]→[2, 3/2, 2] <sup>b</sup>	-5.22	25.16	5	CDMS
Cyclopropenylidene (c-C <sub>3</sub> H <sub>2</sub> )					
244222.15 (0.01)	[3, 2, 1]→[2, 1, 2]	-4.23	18.17	21	CDMS
246557.77 (0.02)	[16, 10, 7]→[16, 9, 8]	-3.36	397.83	99	CDMS
260479.75 (0.02)	[5, 3, 2]→[4, 4, 1]	-3.79	44.72	33	CDMS
Methanol (CH <sub>3</sub> OH $v_t = 0$ )					
243915.79 (0.01)	[5, 1, 4]→[4, 1, 3] A	-4.22	49.66	44	CDMS
246074.61 (0.02)	[20, 3, 17]→[20, 2, 18] A	-4.08	537.03	164	CDMS
246873.30 (0.02)	[19, 3, 16]→[19, 2, 17] A	-4.08	490.65	156	CDMS
261805.68 (0.01)	[2, 1, 1]→[1, 0, 1] E	-4.25	28.01	20	CDMS
Methanol ( <sup>13</sup> CH <sub>3</sub> OH $v_t = 0$ )					
246426.12 (0.22)	[23, 4, 19]→[22, 5, 18]	-4.58	721.02	47	CDMS
247086.3 (0.5)	[23, 3, 20]→[23, 2, 21] A→A+	-4.07	674.86	47	CDMS
259036.49 (0.17)	[17, 3, 15]→[17, 2, 16] A→A-	-4.04	396.48	35	CDMS
Methanol (CH <sub>2</sub> DOH $v_t = 0$ )					
243514.31 (0.01)	[9, 2, 8]→[10, 1, 10] o <sub>1</sub>	-5.17	131.85	19	JPL
246973.11 (0.01)	[4, 1, 4]→[4, 1, 3] e <sub>1</sub>	-4.67	37.69	9	JPL
260543.63 (0.01)	[3, 2, 1]→[3, 1, 2] o <sub>1</sub>	-4.65	48.34	7	JPL
Methanol (CH <sub>3</sub> <sup>18</sup> OH $v_t = 0$ )					
246256.60 (0.04)	[11, 2, 10]→[10, 3, 7] A	-4.64	184.27	92	CDMS
Sulfur monoxide (SO <sup>3</sup> Σ)					
258255.83 (0.01)	[N, J]=[6, 6]→[5, 5]	-3.67	56.50	13	CDMS
261843.72 (0.03)	[N, J]=[7, 6]→[6, 5]	-3.64	47.55	15	CDMS
Sulfur monoxide ( <sup>34</sup> SO)					
246663.47 (0.1)	[N, J]=[5, 6]→[4, 5]	-3.74	49.89	11	CDMS
Sulfur dioxide (SO <sub>2</sub> )					
244254.22 (0.01)	[14, 0, 14]→[13, 1, 13]	-3.79	93.90	29	CDMS
Hydrogen cyanide (H <sup>13</sup> CN)					
259010.26 (0.01)	[J, F]=[3, 3]→[2, 3]	-4.07	24.86	7	CDMS
259011.55 (0.01)	[J, F]=[3, 2]→[2, 1]	-3.19	24.86	5	CDMS
259011.80 (0.01)	[J, F]=[3, 3]→[2, 2]	-3.16	24.86	7	CDMS
259011.86 (0.01)	[J, F]=[3, 4]→[2, 3]	-3.11	24.86	9	CDMS
259012.34 (0.01)	[J, F]=[3, 2]→[2, 3]	-5.46	24.86	5	CDMS
259013.89 (0.01)	[J, F]=[3, 2]→[2, 2]	-3.92	24.86	5	CDMS
Carbon Monosulfide (CS)					
244935.56 (0.01)	[J]=[5]→[4]	-3.53	35.27	11	CDMS
Formaldehyde (HDCO)					
246924.6 (0.1)	[4, 1, 4]→[3, 1, 3]	-3.40	37.60	9	CDMS
259034.9 (0.1)	[4, 2, 2]→[3, 2, 1]	-3.44	62.86	9	CDMS
Methyl formate (HCOOCH <sub>3</sub> )					
245883.2 (0.1)	[20, 13, 7]→[19, 13, 6] E	-3.89	235.98	82	JPL
245885.2 (0.1)	[20, 13, 7]→[19, 13, 6] A	-3.89	235.98	82	JPL
245885.2 (0.1)	[20, 13, 8]→[19, 13, 7] A	-3.89	235.98	82	JPL
245903.7 (0.1)	[20, 13, 8]→[19, 13, 7] E	-3.89	235.97	82	JPL
246027.5 (0.1)	[21, 2, 19]→[20, 3, 18] E	-4.63	139.85	86	JPL
246038.9 (0.1)	[21, 2, 19]→[20, 3, 18] A	-4.63	139.85	86	JPL
246054.8 (0.1)	[20, 12, 8]→[19, 12, 7] E	-3.84	219.43	82	JPL
246060.8 (0.1)	[20, 12, 8/9]→[19, 12, 7/8] A	-3.84	219.43	82	JPL

*Table 6 continued*

**Table 6** (*continued*)

Frequency (MHz)	Transition <sup>a</sup>	log(Einstein-A)	$E_u$ (K)	$g_u$	Ref.
246076.9 (0.1)	[20, 12, 9]→[19, 12, 8] E	-3.84	219.41	82	JPL
246285.4 (0.1)	[20, 11, 9]→[19, 11, 8] E	-3.80	204.21	82	JPL
246295.1 (0.1)	[20, 11, 10]→[19, 11, 9] A	-3.80	204.21	82	JPL
246295.1 (0.1)	[20, 11, 9]→[19, 11, 8] A	-3.80	204.21	82	JPL
246308.3 (0.1)	[20, 11, 10]→[19, 11, 9] E	-3.80	204.20	82	JPL
246456.1 (0.1)	[10, 5, 6]→[9, 4, 5] E	-5.52	49.09	42	JPL
246600.0 (0.1)	[20, 10, 10]→[19, 10, 9] E	-3.77	190.34	82	JPL
246613.4 (0.1)	[20, 10, 11]→[19, 10, 10] A	-3.77	190.34	82	JPL
246613.4 (0.1)	[20, 10, 10]→[19, 10, 9] A	-3.77	190.34	82	JPL
246623.2 (0.1)	[20, 10, 11]→[19, 10, 10] E	-3.77	190.34	82	JPL
246660.5 (0.1)	[10, 5, 6]→[9, 4, 5] A	-4.74	49.08	42	JPL
246675.4 (0.1)	[15, 4, 12]→[14, 3, 11] E	-4.93	81.85	62	JPL
246683.5 (0.1)	[15, 4, 12]→[14, 3, 11] A	-4.93	81.84	62	JPL
246752.9 (0.1)	[10, 5, 5]→[9, 4, 5] E	-4.90	49.10	42	JPL
246891.6 (0.1)	[19, 4, 15]→[18, 4, 14] E	-3.66	126.22	78	JPL
246914.7 (0.1)	[19, 4, 15]→[18, 4, 14] A	-3.66	126.22	78	JPL
246945.7 (0.1)	[10, 5, 6]→[9, 4, 6] E	-4.90	49.09	42	JPL
247040.7 (0.1)	[20, 9, 11]→[19, 9, 10] E	-3.74	177.83	82	JPL
247044.1 (0.1)	[21, 3, 19]→[20, 3, 18] E	-3.66	139.90	86	JPL
247053.5 (0.1)	[21, 3, 19]→[20, 3, 18] A	-3.66	139.89	86	JPL
247057.3 (0.1)	[20, 9, 12]→[19, 9, 11] A	-3.74	177.83	82	JPL
247057.7 (0.1)	[20, 9, 11]→[19, 9, 10] A	-3.74	177.83	82	JPL
247063.7 (0.1)	[20, 9, 12]→[19, 9, 11] E	-3.74	177.83	82	JPL
247124.3 (0.1)	[10, 5, 5]→[9, 4, 6] E	-4.74	49.08	42	JPL
258275.0 (0.1)	[21, 13, 8]→[20, 13, 7] E	-3.79	248.37	86	JPL
258277.4 (0.1)	[21, 13, 8]→[20, 13, 7] A	-3.79	248.37	86	JPL
258277.4 (0.1)	[21, 13, 9]→[20, 13, 8] A	-3.79	248.37	86	JPL
259341.9 (0.1)	[24, 0, 24]→[23, 1, 23] E	-4.37	158.23	98	JPL
259342.0 (0.1)	[24, 1, 24]→[23, 1, 23] E	-3.58	158.23	98	JPL
259342.1 (0.1)	[24, 0, 24]→[23, 0, 23] E	-3.58	158.23	98	JPL
259342.3 (0.1)	[24, 1, 24]→[23, 0, 23] E	-4.37	158.23	98	JPL
259342.7 (0.1)	[24, 0, 24]→[23, 1, 23] A	-4.37	158.22	98	JPL
259342.9 (0.1)	[24, 1, 24]→[23, 1, 23] A	-3.58	158.22	98	JPL
259343.0 (0.1)	[24, 0, 24]→[23, 0, 23] A	-3.58	158.22	98	JPL
259343.2 (0.1)	[24, 1, 24]→[23, 0, 23] A	-4.37	158.22	98	JPL
261822.3 (0.1)	[17, 10, 7]→[17, 9, 8] A	-4.73	156.63	70	JPL
262088.2 (0.1)	[16, 10, 6]→[16, 9, 7] A	-4.76	146.59	66	JPL
262088.2 (0.1)	[16, 10, 7]→[16, 9, 8] A	-4.76	146.59	66	JPL
Methyl formate (HCOOCH <sub>3</sub> $v = 1$ )					
243511.5 (0.1)	[20, 12, 8]→[19, 12, 7] E	-3.85	407.25	82	JPL
245846.9 (0.1)	[21, 3, 19]→[20, 3, 18] E	-3.66	326.30	86	JPL
246106.8 (0.1)	[20, 7, 14]→[19, 7, 13] A	-3.70	343.77	82	JPL
246184.2 (0.1)	[20, 8, 13]→[19, 8, 12] E	-3.72	353.27	82	JPL
246187.0 (0.1)	[21, 2, 19]→[20, 2, 18] A	-3.66	326.62	86	JPL
246233.6 (0.1)	[20, 7, 13]→[19, 7, 12] A	-3.70	343.79	82	JPL
246274.9 (0.1)	[20, 7, 13]→[19, 7, 12] E	-3.70	343.86	82	JPL
246410.95 (0.01)	[10, 5, 5]→[9, 4, 6] A	-4.73	236.70	42	JPL
246422.7 (0.1)	[22, 1, 21]→[21, 2, 20] A	-4.51	330.43	90	JPL
246461.2 (0.1)	[22, 2, 21]→[21, 2, 20] A	-3.65	330.43	90	JPL
246488.4 (0.1)	[22, 1, 21]→[21, 1, 20] A	-3.65	330.43	90	JPL
246562.9 (0.1)	[21, 2, 19]→[20, 2, 18] E	-3.66	326.24	86	JPL
246706.5 (0.1)	[22, 2, 21]→[21, 2, 20] E	-3.65	329.89	90	JPL
246731.7 (0.1)	[22, 1, 21]→[21, 1, 20] E	-3.65	329.89	90	JPL
246985.2 (0.1)	[20, 6, 15]→[19, 6, 14] A	-3.68	335.37	82	JPL

Table 6 continued

**Table 6** (*continued*)

Frequency (MHz)	Transition <sup>a</sup>	log(Einstein-A)	<i>E<sub>u</sub></i> (K)	<i>g<sub>u</sub></i>	Ref.
259003.9 (0.1)	[21, 7, 14]→[20, 7, 13] A	-3.63	356.22	86	JPL
259025.8 (0.1)	[21, 7, 14]→[20, 7, 13] E	-3.63	356.29	86	JPL
260479.6 (0.1)	[44, 9, 36]→[44, 8, 37] A	-4.59	828.74	178	JPL
Dimethyl ether (CH <sub>3</sub> OCH <sub>3</sub> )					
246499.29 (0.01)	[37, 6, 31]→[37, 5, 12] AA	-4.01	693.72	750	CDMS
246505.09 (0.01)	[37, 6, 31]→[37, 5, 12] AE	-4.01	693.72	450	CDMS
246505.09 (0.01)	[37, 6, 31]→[37, 5, 12] EA	-4.01	693.72	300	CDMS
246697.43 (0.01)	[27, 4, 23]→[26, 5, 21] AA	-4.70	367.61	330	CDMS
246697.87 (0.01)	[27, 4, 23]→[26, 5, 21] EE	-4.70	367.61	880	CDMS
246698.31 (0.01)	[27, 4, 23]→[26, 5, 21] AE	-4.70	367.61	110	CDMS
246698.31 (0.01)	[27, 4, 23]→[26, 5, 21] EA	-4.70	367.61	220	CDMS
259305.22 (0.01)	[33, 3, 31]→[34, 6, 28] AA	-6.61	563.02	670	CDMS
259308.39 (0.01)	[33, 3, 31]→[34, 6, 28] AE	-6.61	563.02	402	CDMS
259308.39 (0.01)	[33, 3, 31]→[34, 6, 28] EA	-6.61	563.02	268	CDMS
259309.47 (0.01)	[17, 5, 12]→[17, 4, 13] AE	-4.06	174.54	210	CDMS
259309.76 (0.01)	[17, 5, 12]→[17, 4, 13] EA	-4.06	174.54	140	CDMS
259311.95 (0.01)	[17, 5, 12]→[17, 4, 13] EE	-4.06	174.54	560	CDMS
259314.28 (0.01)	[17, 5, 12]→[17, 4, 13] AA	-4.06	174.54	350	CDMS
Acetone (CH <sub>3</sub> COCH <sub>3</sub> )					
244218.91 (0.01)	[20, 5, 15]→[19, 6, 14] AE	-3.32	139.69	82	JPL
244218.91 (0.01)	[20, 6, 15]→[19, 5, 14] AE	-3.32	139.69	250	JPL
244218.92 (0.01)	[20, 5, 15]→[19, 6, 14] EA	-3.32	139.69	160	JPL
244218.92 (0.01)	[20, 6, 15]→[19, 5, 14] EA	-3.32	139.69	160	JPL
245831.34 (0.09)	[13, 10, 3]→[12, 9, 4] EE	-3.80	77.84	432	JPL
246400.99 (0.05)	[34, 7, 28]→[34, 5, 29] EE	-4.17	364.98	1100	JPL
246400.99 (0.05)	[34, 6, 28]→[34, 5, 29] EE	-4.03	364.98	1100	JPL
246400.99 (0.05)	[34, 7, 28]→[34, 6, 29] EE	-4.03	364.98	1100	JPL
246400.99 (0.05)	[34, 6, 28]→[34, 6, 29] EE	-4.17	364.98	1100	JPL
246404.27 (0.01)	[22, 3, 19]→[21, 4, 18] AE	-3.23	149.62	90	JPL
246404.27 (0.01)	[22, 4, 19]→[21, 3, 18] AE	-3.23	149.62	270	JPL
246404.29 (0.01)	[22, 3, 19]→[21, 4, 18] EA	-3.23	149.62	180	JPL
246404.29 (0.01)	[22, 4, 19]→[21, 3, 18] EA	-3.23	149.62	180	JPL
246450.40 (0.01)	[22, 4, 19]→[21, 3, 18] EE	-3.23	149.57	720	JPL
246450.40 (0.01)	[22, 3, 19]→[21, 3, 18] EE	-5.09	149.57	720	JPL
246450.40 (0.01)	[22, 3, 19]→[21, 4, 18] EA	-3.24	149.57	720	JPL
246450.40 (0.01)	[22, 4, 19]→[21, 4, 18] EA	-4.92	149.57	720	JPL
246496.17 (0.46)	[25, 14, 12]→[24, 15, 9] AE	-5.01	257.11	100	JPL
246496.47 (0.02)	[22, 3, 19]→[21, 4, 18] AA	-3.23	149.51	270	JPL
246496.47 (0.02)	[22, 4, 19]→[21, 3, 18] AA	-3.23	149.51	450	JPL
246714.12 (0.05)	[9, 8, 1]→[8, 5, 4] EA	-5.84	40.59	76	JPL
246714.94 (0.05)	[32, 4, 28]→[32, 4, 29] EA	-3.97	305.61	260	JPL
246714.94 (0.05)	[32, 5, 28]→[32, 3, 29] EA	-3.97	305.61	260	JPL
246715.04 (0.05)	[32, 5, 28]→[32, 4, 29] AE	-3.97	305.61	390	JPL
246715.04 (0.05)	[32, 4, 28]→[32, 3, 29] EA	-3.97	305.61	130	JPL
246719.92 (0.04)	[33, 6, 28]→[33, 4, 29] EE	-5.62	344.85	1100	JPL
246719.92 (0.04)	[33, 5, 28]→[33, 4, 29] EE	-3.87	344.85	1100	JPL
246719.92 (0.04)	[33, 6, 28]→[33, 5, 29] EE	-3.87	344.85	1100	JPL
246719.92 (0.04)	[33, 5, 28]→[33, 5, 29] EE	-5.61	344.85	1100	JPL
261818.11 (0.01)	[20, 7, 13]→[19, 8, 12] EA	-3.31	151.17	160	JPL
261818.17 (0.01)	[20, 7, 13]→[19, 8, 12] AE	-3.31	151.17	82	JPL
261819.09 (0.01)	[20, 8, 13]→[19, 7, 12] EA	-3.31	151.17	160	JPL
261819.17 (0.01)	[20, 8, 13]→[19, 7, 12] AE	-3.31	151.17	250	JPL
Methyl cyanide (CH <sub>3</sub> CN)					
257507.56 (0.01)	[ <i>N</i> , <i>K</i> ]=[14, 2]→[13, 2]	-3.00	121.28	58	JPL

*Table 6 continued*

**Table 6** (*continued*)

Frequency (MHz)	Transition <sup>a</sup>	log(Einstein-A)	$E_u$ (K)	$g_u$	Ref.
257522.43 (0.01)	[ $N, K$ ]=[14, 1]→[13, 1]	-2.99	99.84	58	JPL
257527.38 (0.01)	[ $N, K$ ]=[14, 0]→[13, 0]	-2.99	92.70	58	JPL
Acetaldehyde ( $\text{CH}_3\text{CHO}$ $v_t = 0$ )					
246330.73 (0.01)	[15, 3, 13]→[15, 2, 14] A	-4.29	131.49	62	JPL
260530.40 (0.01)	[14, 1, 14]→[13, 1, 13] E	-3.20	96.39	58	JPL
260544.02 (0.01)	[14, 1, 14]→[13, 1, 13] A	-3.20	96.32	58	JPL
260547.46 (2.07)	[9, 4, 5]→[9, 3, 7] E, $v_t = 2$	-6.06	456.38	38	JPL
gauche-Ethanol ( $g\text{-C}_2\text{H}_5\text{OH}$ )					
246414.76 (0.05)	[14, 3, 11]→[13, 3, 10] $v_t = 0 \rightarrow 0$	-3.89	155.72	29	JPL
246524.28 (0.01)	[13, 2, 12]→[12, 1, 12] $v_t = 0 \rightarrow 1$	-4.50	136.95	27	JPL
246658.18 (0.01)	[32, 5, 28]→[32, 4, 29] $v_t = 0 \rightarrow 0$	-6.33	527.94	65	JPL
246662.98 (0.01)	[4, 2, 3]→[3, 1, 3] $v_t = 1 \rightarrow 0$	-4.36	74.77	9	JPL
259322.64 (0.01)	[14, 3, 11]→[13, 2, 11] $v_t = 0 \rightarrow 1$	-4.39	155.72	29	JPL
260457.73 (0.01)	[15, 4, 12]→[14, 4, 11] $v_t = 1 \rightarrow 1$	-3.83	181.10	31	JPL
trans-Ethanol ( $\text{C}_2\text{H}_5\text{OH}$ )					
246663.62 (0.05)	[24, 1, 23]→[24, 0, 24]	-3.73	252.35	49	JPL
261815.99 (0.05)	[28, 3, 26]→[28, 2, 27]	-3.96	350.98	57	JPL
Glycolaldehyde ( $cis\text{-CH}_2\text{OHCHO}$ )					
246773.09 (0.02)	[30, 2, 28]→[30, 1, 29]	-4.04	252.68	61	CDMS
246778.28 (0.02)	[30, 3, 28]→[30, 2, 29]	-4.04	252.68	61	CDMS
262056.78 (0.01)	[25, 2, 24]→[24, 1, 23]	-3.34	158.25	51	CDMS
261795.48 (0.01)	[25, 11, 14]→[25, 10, 15]	-3.57	254.23	51	CDMS
261798.96 (0.01)	[25, 11, 15]→[25, 10, 16]	-3.57	254.23	51	CDMS
Methyl cyanide ( $\text{CH}_2\text{DCN}$ )					
259315.51 (0.01)	[15, 1, 15]→[14, 1, 14]	-2.82	104.97	31	CDMS
260523.05 (0.01)	[15, 2, 13]→[14, 2, 12]	-2.82	121.60	31	CDMS
Ethyl cyanide ( $\text{CH}_3\text{CH}_2\text{CN}$ )					
246268.74 (0.01)	[27, 2, 25]→[26, 2, 24]	-2.90	169.80	55	CDMS
246421.92 (0.01)	[28, 2, 27]→[27, 2, 26]	-2.90	177.26	57	CDMS
246548.70 (0.01)	[27, 3, 24]→[26, 3, 23]	-2.90	174.06	55	CDMS
260535.69 (0.05)	[29, 5, 25]→[28, 5, 24]	-2.84	215.06	59	CDMS
Formamide ( $\text{NH}_2\text{CHO}$ )					
243521.04 (0.01)	[12, 1, 12]→[11, 1, 11]	-2.98	79.19	25	CDMS
Formic acid ( $t\text{-HCOOH}$ )					
262103.48 (0.01)	[12, 0, 12]→[11, 0, 11]	-3.69	82.77	25	CDMS

<sup>a</sup>The typical quantum numbers are listed as [ $J, K_a, K_c$ ] unless specified.

<sup>b</sup>The quantum numbers are [ $N, J, F$ ]

#### D. THE SPECTRA OF $\text{C}_2\text{H}$

#### C. INTENSITY MAPS OF $\text{CH}_3\text{OH}$ , $\text{CH}_3\text{CN}$ , $\text{HCOOCH}_3$ , AND $\text{CH}_3\text{OCH}_3$

Figure 15 shows the intensity maps of  $\text{CH}_3\text{OH}$ ,  $\text{CH}_3\text{CN}$ ,  $\text{HCOOCH}_3$ , and  $\text{CH}_3\text{OCH}_3$  for the PEACHES sources not shown in Figure 2.

The  $\text{C}_2\text{H}$  spectra toward the continuum emission have irregular line profiles. Some spectra have strong self-absorption, while some spectra only show the blue-shifted emission. Due to the absorption and irregular line profile, the xCLASS fitting routine often fails to faithfully reproduce the observed  $\text{C}_2\text{H}$  spectra.  $\text{C}_2\text{H}$  can easily form in the outflow cavity wall due to the abundant  $\text{CH}_4$  sublimated from dust grains as well as  $\text{C}^+$  ionized by the UV radiation. Thus, the  $\text{C}_2\text{H}$  spectra can have broad line width and multiple components. Furthermore, the morphology of the  $\text{C}_2\text{H}$  emission traces the outflows, making our extraction from the continuum emission non-ideal for representing the nature of

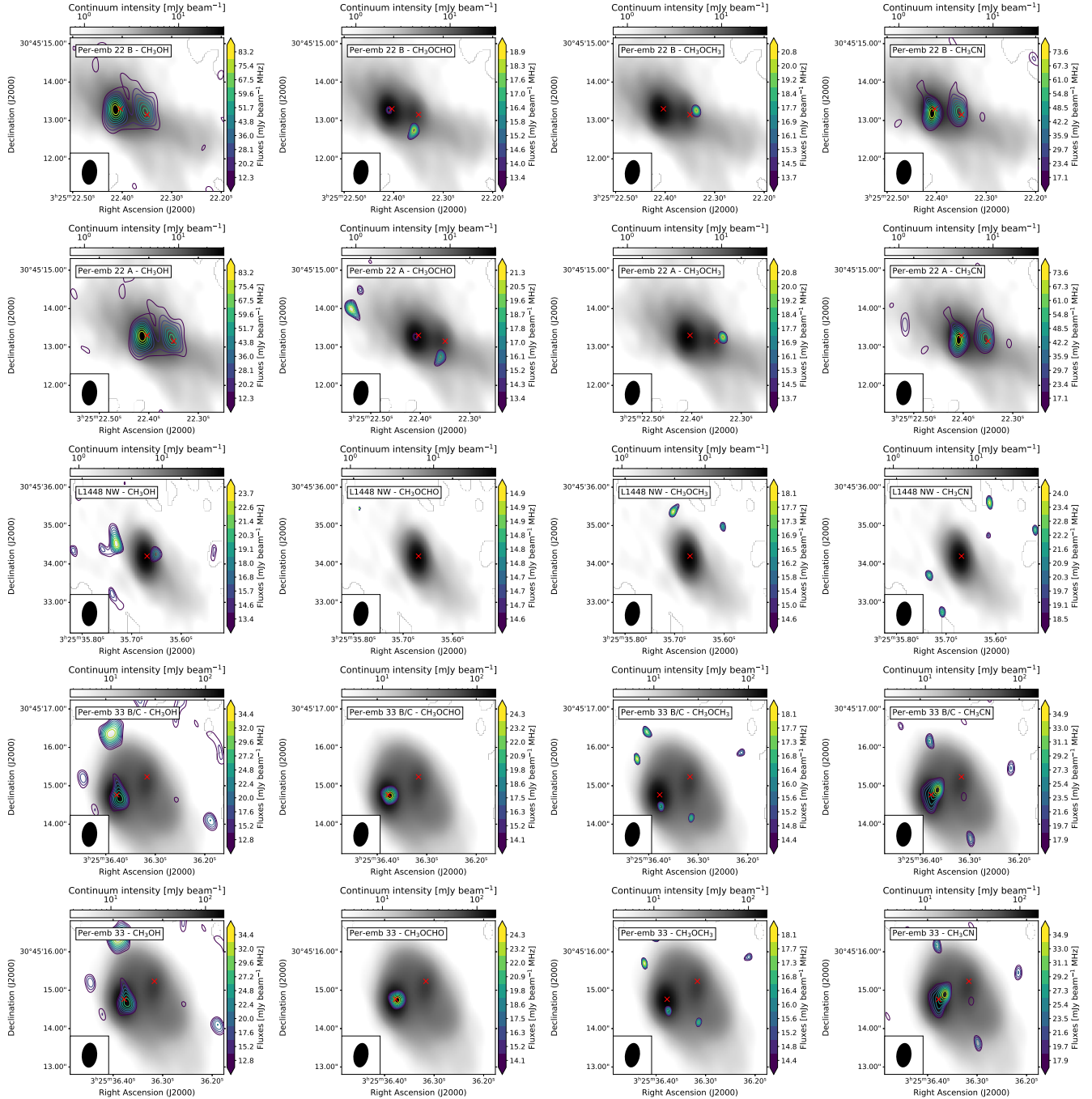


**Figure 15.** The intensity maps of most detected COMs, CH<sub>3</sub>OH, CH<sub>3</sub>CN, HCOOCH<sub>3</sub>, and CH<sub>3</sub>OCH<sub>3</sub> (from left to right). Each row shows the emission of a PEACHES protostar with increasing R.A. The intensity is calculated by integrating over 3 km s<sup>-1</sup> around the line centroid, while the lowest contour shows the 3 $\sigma$  value. The grayscale images illustrate the continuum emission.

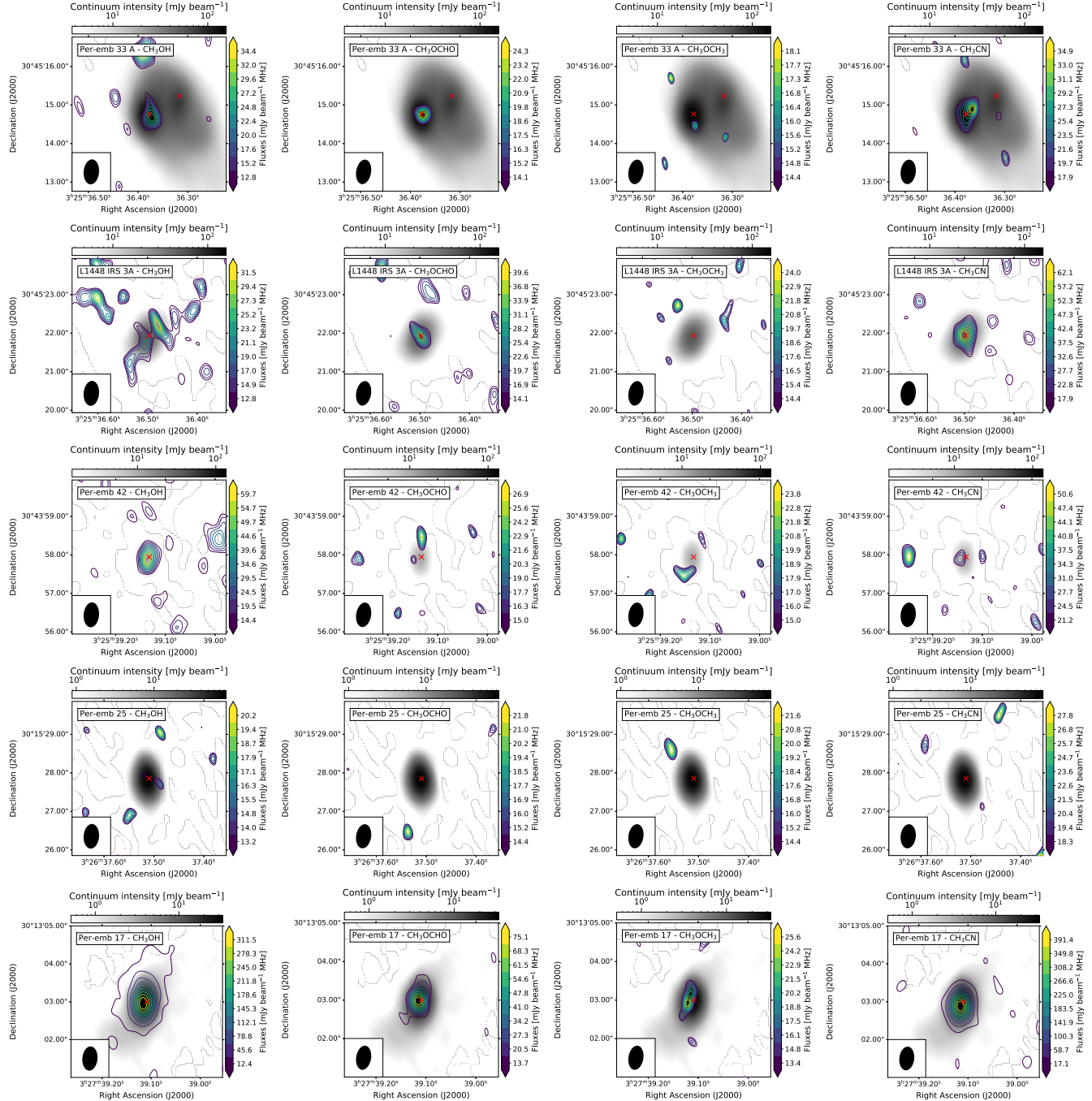


Figure 15 (Cont.).

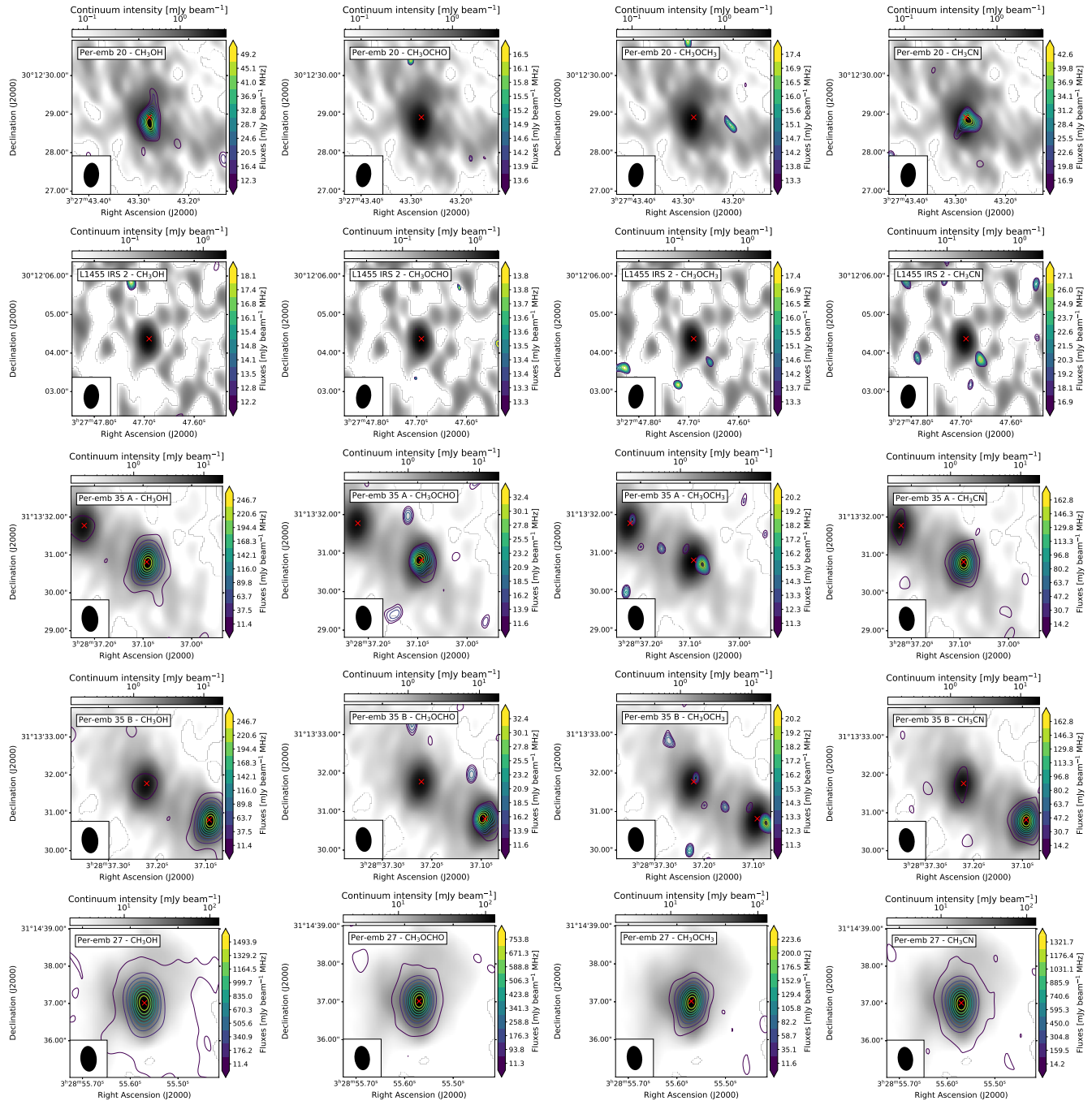


Figure 15 (Cont.).

the C<sub>2</sub>H emission. Figure 17 and Y show the spectra and the moment 0 map of C<sub>2</sub>H, respectively.

## REFERENCES

- Aikawa, Y. 2013, Chemical Reviews, 113, 8961  
 Astropy Collaboration, Price-Whelan, A. M., Sipőcz, B. M., et al. 2018, AJ, 156, 123

- Belloche, A., Maury, A. J., Maret, S., et al. 2020, A&A, 635, A198  
 Belov, S. P., Tretyakov, M. Y., Kozin, I. N., et al. 1998, Journal of Molecular Spectroscopy, 191, 17

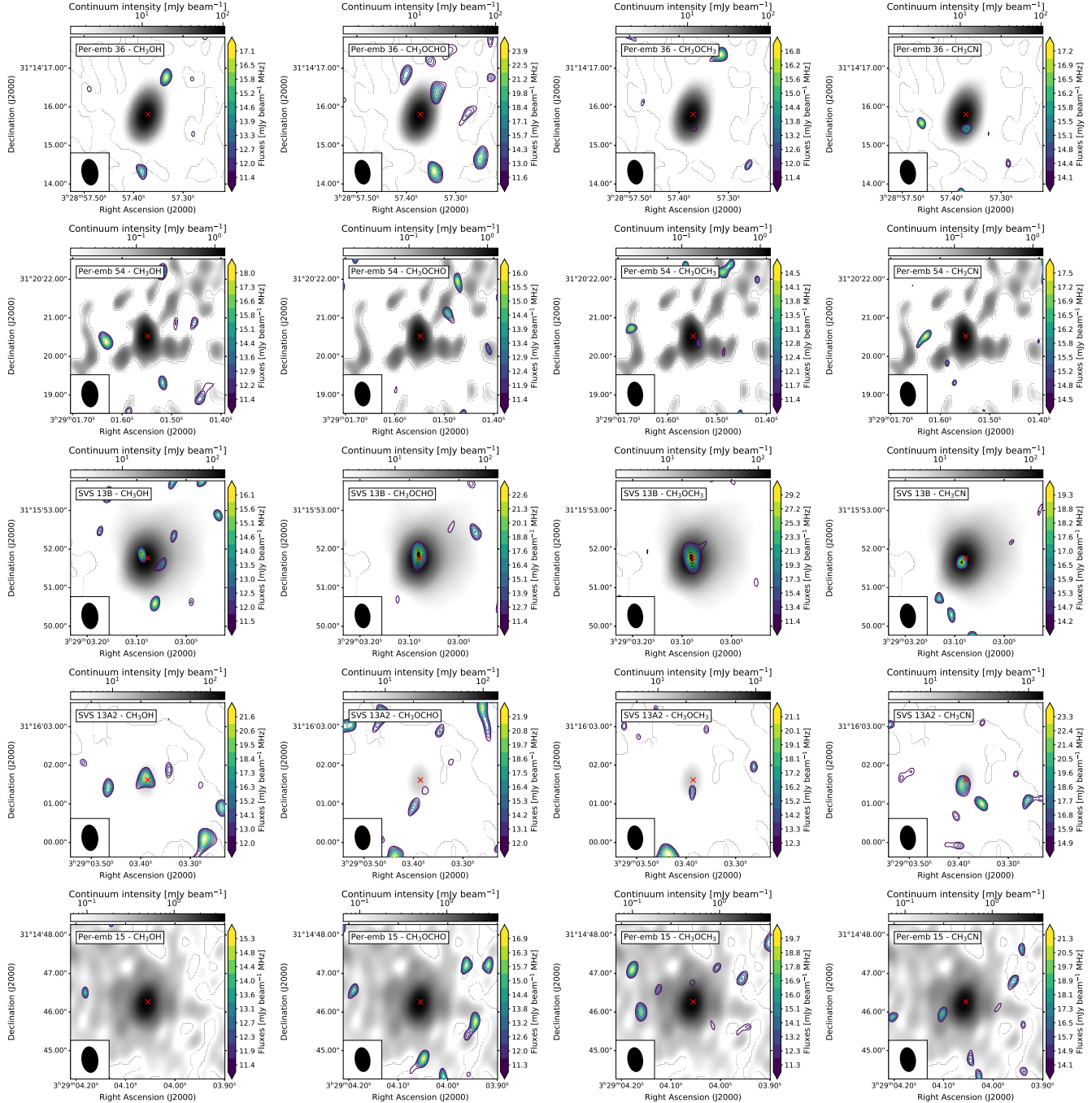


Figure 15 (Cont.).

Bergner, J. B., Öberg, K. I., Garrod, R. T., & Graninger, D. M. 2017, ApJ, 841, 120

Bottinelli, S., Ceccarelli, C., Williams, J. P., & Lefloch, B. 2007, A&A, 463, 601

Bottinelli, S., Ceccarelli, C., Lefloch, B., et al. 2004, ApJ, 615, 354

Brauer, C. S., Pearson, J. C., Drouin, B. J., & Yu, S. 2009, ApJS, 184, 133

Calcutt, H., Jørgensen, J. K., Müller, H. S. P., et al. 2018, A&A, 616, A90

Carney, M. T., Yıldız, U. A., Mottram, J. C., et al. 2016, A&A, 586, A44

Carvajal, M., Willaert, F., Demaison, J., & Kleiner, I. 2007, Journal of Molecular Spectroscopy, 246, 158

Cazaux, S., Tielens, A. G. G. M., Ceccarelli, C., et al. 2003, ApJL, 593, L51

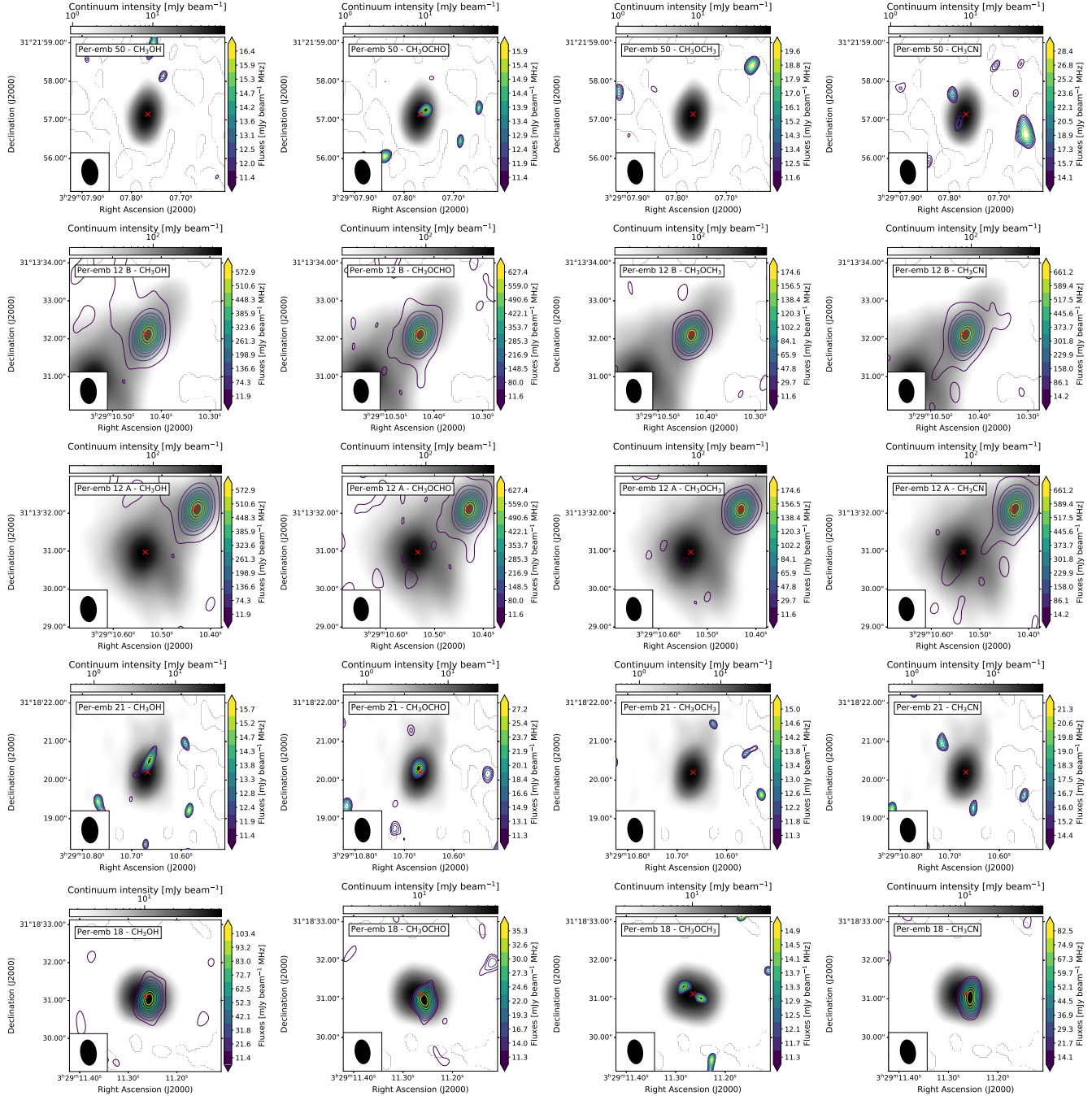


Figure 15 (Cont.).

Ceccarelli, C. 2004, in Astronomical Society of the Pacific Conference Series, Vol. 323, Star Formation in the Interstellar Medium: In Honor of David Hollenbach, ed. D. Johnstone, F. C. Adams, D. N. C. Lin, D. A. Neufeld, & E. C. Ostriker, 195

Curtis, E. I., Richer, J. S., Swift, J. J., & Williams, J. P. 2010, MNRAS, 408, 1516

De Simone, M., Ceccarelli, C., Codella, C., et al. 2020, ApJL, 896, L3

Dunham, M. M., Arce, H. G., Allen, L. E., et al. 2013, AJ, 145, 94

Endres, C. P., Drouin, B. J., Pearson, J. C., et al. 2009, A&A, 504, 635

Endres, C. P., Schlemmer, S., Schilke, P., Stutzki, J., & Müller, H. S. P. 2016, Journal of Molecular Spectroscopy, 327, 95

Garrod, R. T. 2013, ApJ, 765, 60

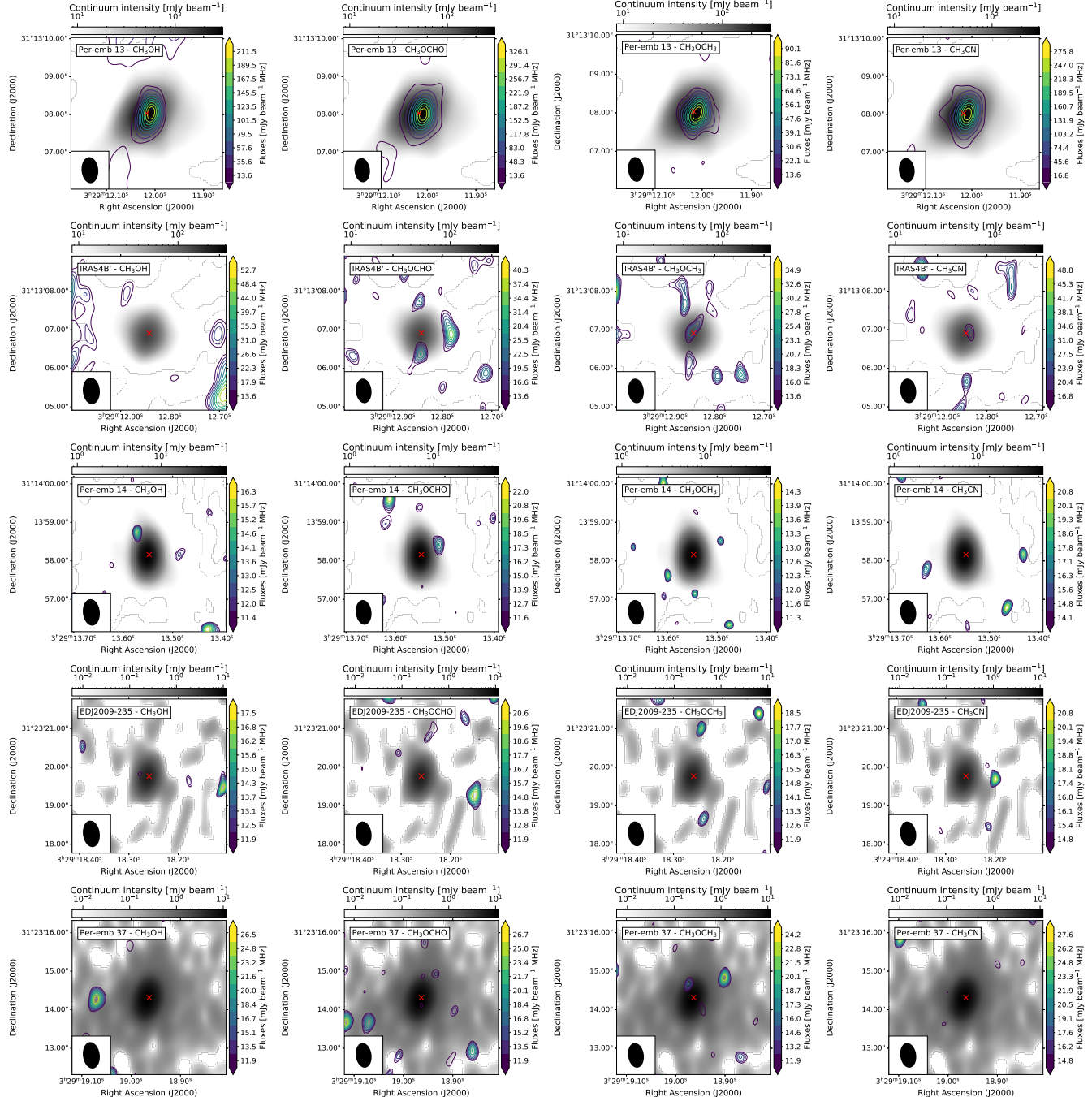


Figure 15 (Cont.).

Garrod, R. T., Widicus Weaver, S. L., & Herbst, E. 2008, ApJ, 682, 283

Gerin, M., Pety, J., Commerçon, B., et al. 2017, A&A, 606, A35

Graninger, D. M., Wilkins, O. H., & Öberg, K. I. 2016, ApJ, 833, 125

Gratier, P., Majumdar, L., Ohishi, M., et al. 2016, ApJS, 225, 25

Groner, P., Albert, S., Herbst, E., et al. 2002, ApJS, 142, 145

Hatchell, J., Fuller, G. A., Richer, J. S., Harries, T. J., & Ladd, E. F. 2007, A&A, 468, 1009

Hatchell, J., Richer, J. S., Fuller, G. A., et al. 2005, A&A, 440, 151

Helmlinger, P. A., & De Lucia, F. C. 1985, Journal of Molecular Spectroscopy, 111, 66

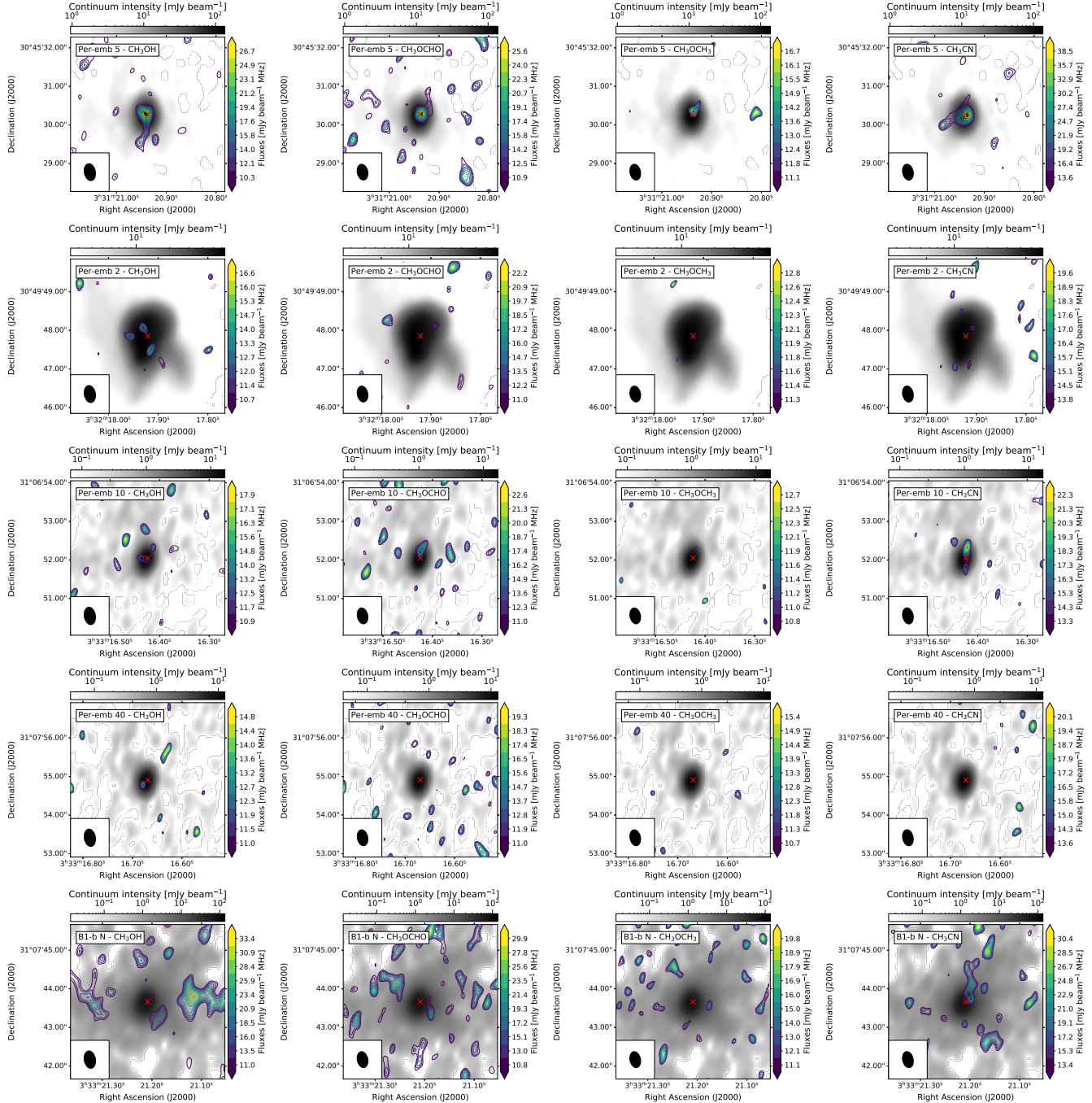


Figure 15 (Cont.).

Higuchi, A. E., Sakai, N., Watanabe, Y., et al. 2018, ApJS, 236, 52

Hirota, T., Bushimata, T., Choi, Y. K., et al. 2008, PASJ, 60, 37

Ilyushin, V., Kryvda, A., & Alekseev, E. 2009, Journal of Molecular Spectroscopy, 255, 32

Imai, M., Oya, Y., Sakai, N., et al. 2019, ApJL, 873, L21

Imai, M., Sakai, N., Oya, Y., et al. 2016, ApJL, 830, L37

Jacobsen, S. K., Jørgensen, J. K., Di Francesco, J., et al. 2019, A&A, 629, A29

Jørgensen, J. K., Belloche, A., & Garrod, R. T. 2020, arXiv e-prints, arXiv:2006.07071

Jørgensen, J. K., Johnstone, D., Kirk, H., et al. 2008, ApJ, 683, 822

Jørgensen, J. K., van der Wiel, M. H. D., Coutens, A., et al. 2016, A&A, 595, A117

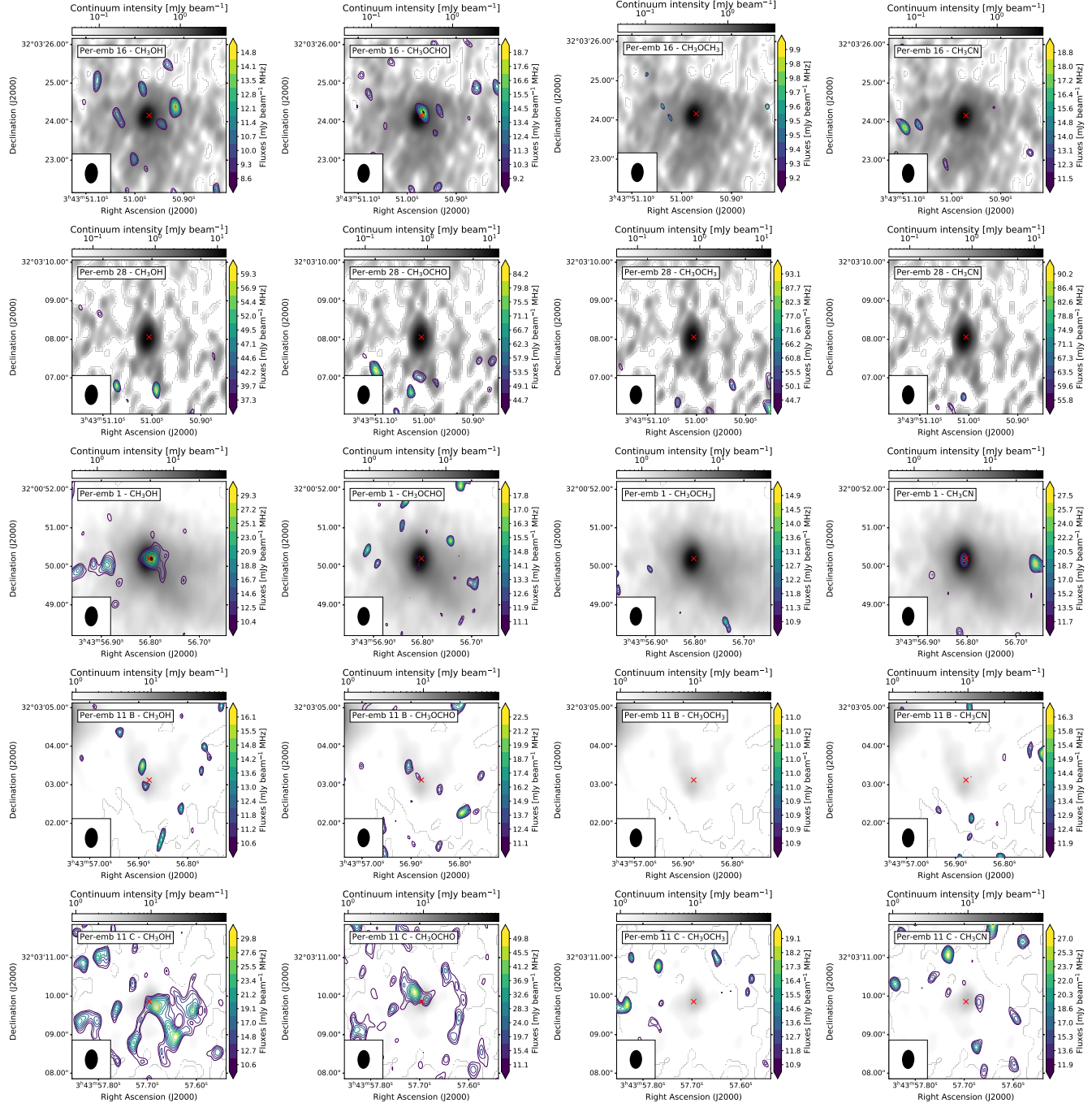


Figure 15 (Cont.).

- Jørgensen, J. K., Müller, H. S. P., Calcutt, H., et al. 2018, *A&A*, 620, A170  
 Kleiner, I., Lovas, F. J., & Godefroid, M. 1996, *Journal of Physical and Chemical Reference Data*, 25, 1113  
 Ko, C.-L., Liu, H. B., Lai, S.-P., et al. 2020, *ApJ*, 889, 172  
 Law, C. J., Öberg, K. I., Bergner, J. B., & Graninger, D. 2018, *ApJ*, 863, 88  
 Lee, C.-F., Hirano, N., Palau, A., et al. 2009, *ApJ*, 699, 1584

- Lee, C.-F., Li, Z.-Y., Ho, P. T. P., et al. 2017, *ApJ*, 843, 27  
 Lovas, F. J. 1985, *Journal of Physical and Chemical Reference Data*, 14, 395  
 Maeda, A., De Lucia, F. C., & Herbst, E. 2008, *Journal of Molecular Spectroscopy*, 251, 293  
 Manigand, S., Jørgensen, J. K., Calcutt, H., et al. 2020, *A&A*, 635, A48  
 Marcelino, N., Gerin, M., Cernicharo, J., et al. 2018, *A&A*, 620, A80

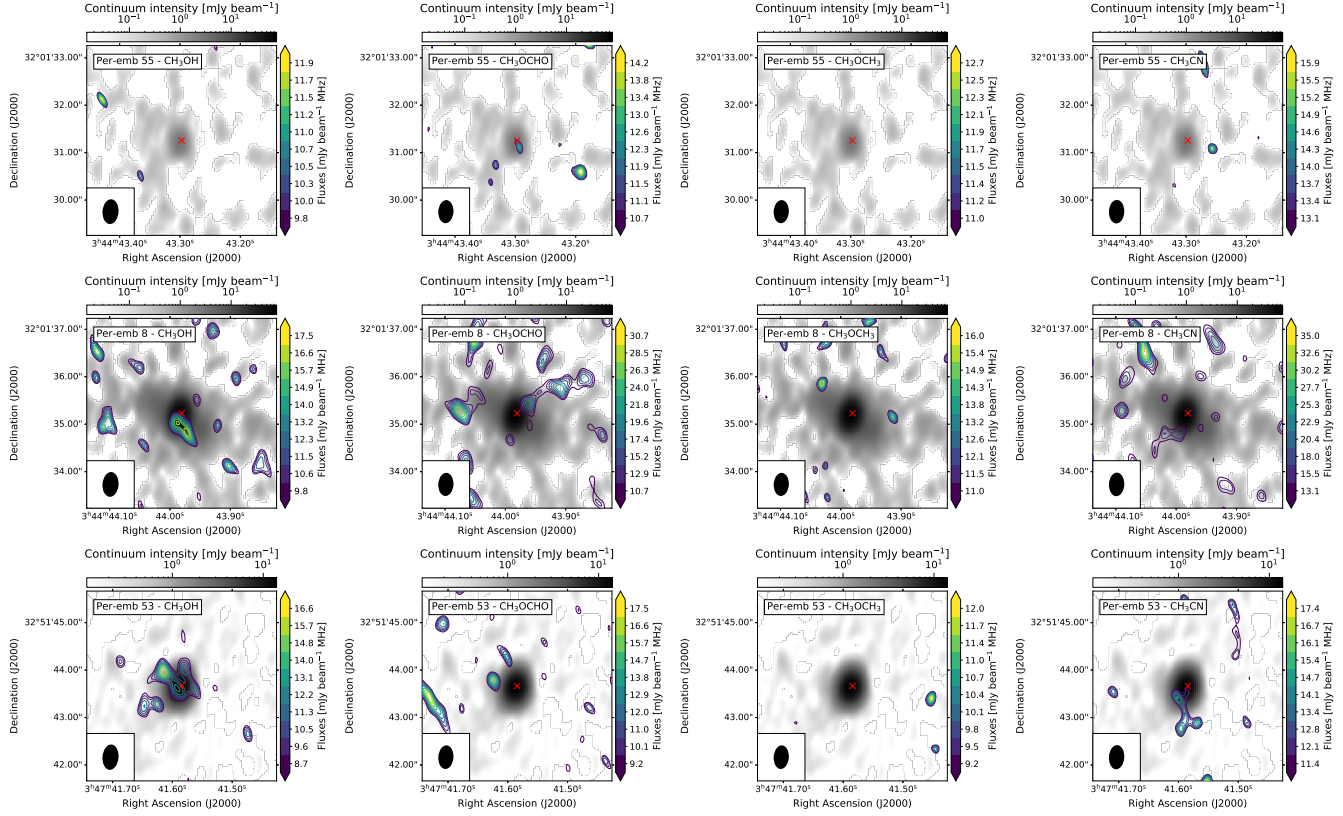
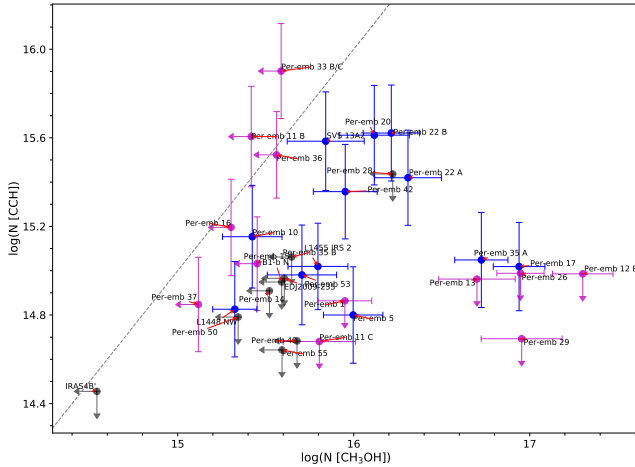


Figure 15 (Cont.).



**Figure 16.** Correlation of the column densities of  $\text{C}_2\text{H}$  and  $\text{CH}_3\text{OH}$  fitted from the PEACHES protostars. The sources where both molecules are detected are shown in black; the sources where only one molecule is detected are shown in magenta; finally, the sources where both molecules are not detected are shown in black for the corresponding upper limits.

McGuire, B. A. 2018, ApJS, 239, 17

- McMullin, J. P., Waters, B., Schiebel, D., Young, W., & Golap, K. 2007, in Astronomical Society of the Pacific Conference Series, Vol. 376, Astronomical Data Analysis Software and Systems XVI, ed. R. A. Shaw, F. Hill, & D. J. Bell, 127
- Möller, T., Endres, C., & Schilke, P. 2017, A&A, 598, A7
- Müller, H. S. P., & Brünken, S. 2005, Journal of Molecular Spectroscopy, 232, 213
- Müller, H. S. P., Drouin, B. J., & Pearson, J. C. 2009, A&A, 506, 1487
- Müller, H. S. P., Schlöder, F., Stutzki, J., & Winnewisser, G. 2005, Journal of Molecular Structure, 742, 215
- Müller, H. S. P., Thorwirth, S., Roth, D. A., & Winnewisser, G. 2001, A&A, 370, L49
- Murillo, N. M., van Dishoeck, E. F., Tobin, J. J., & Fedele, D. 2016, A&A, 592, A56
- Nagy, Z., Spezzano, S., Caselli, P., et al. 2019, A&A, 630, A136
- Oesterling, L. C., Albert, S., De Lucia, F. C., Sastry, K. V. L. N., & Herbst, E. 1999, ApJ, 521, 255
- Ortiz-León, G. N., Loinard, L., Dzib, S. A., et al. 2018, ApJ, 865, 73
- Oya, Y., Sakai, N., López-Sepulcre, A., et al. 2016, ApJ, 824, 88
- Oya, Y., Sakai, N., Watanabe, Y., et al. 2017, ApJ, 837, 174

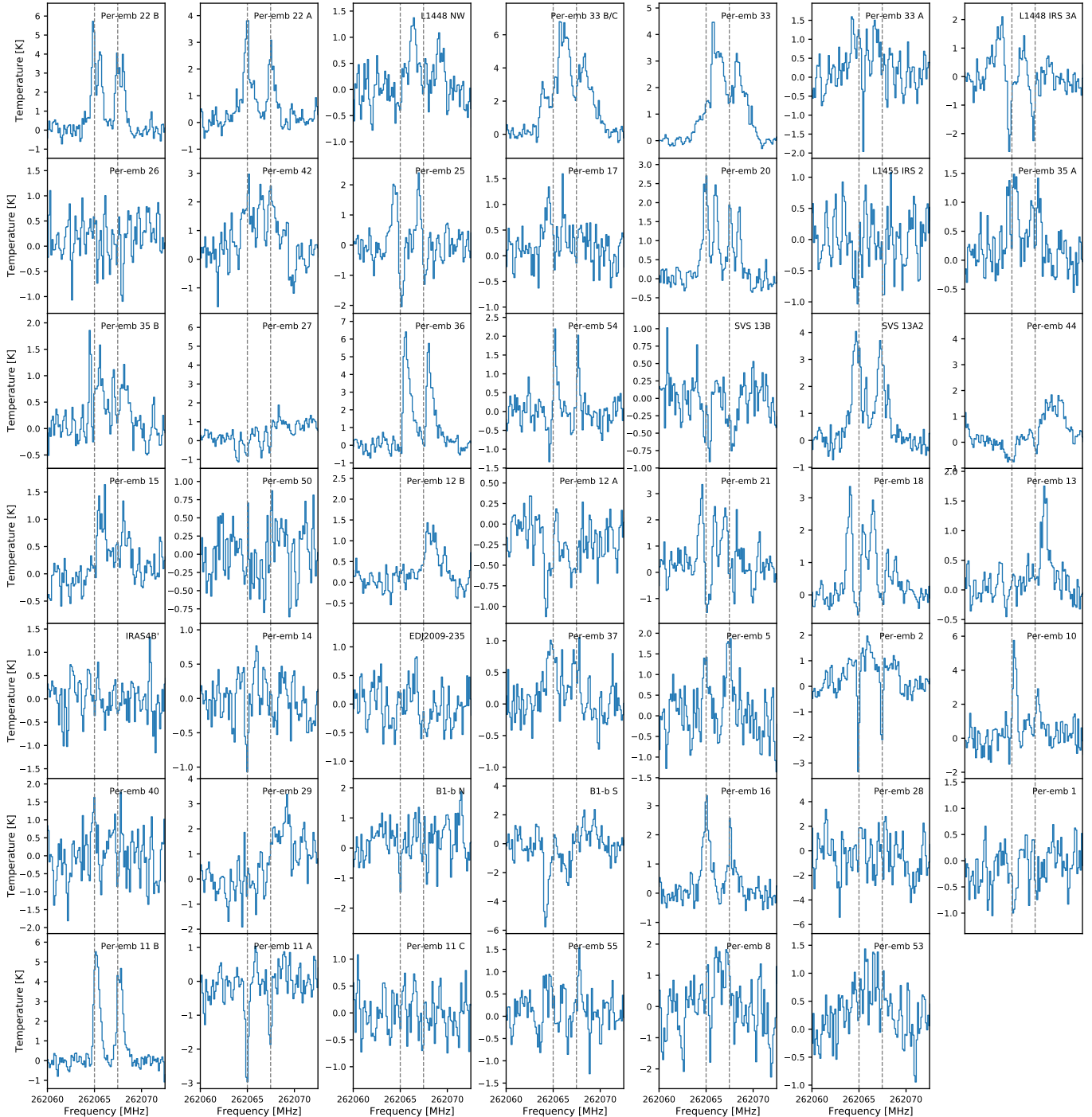


**Figure 17.** The  $\text{C}_2\text{H}$  spectra of all PEACHES sources extracted from the continuum emission.

Pearson, J. C., Brauer, C. S., & Drouin, B. J. 2008, Journal of Molecular Spectroscopy, 251, 394

Pearson, J. C., & Mueller, H. S. P. 1996, ApJ, 471, 1067

Pearson, J. C., Sastry, K. V. L. N., Herbst, E., & De Lucia, F. C. 1994, ApJS, 93, 589

—. 1996, Journal of Molecular Spectroscopy, 175, 246

Pearson, J. C., Yu, S., & Drouin, B. J. 2012, Journal of Molecular Spectroscopy, 280, 119

Pickett, H. M., Poynter, R. L., Cohen, E. A., et al. 1998, JQSRT, 60, 883

Plummer, G. M., Herbst, E., De Lucia, F., & Blake, G. A. 1984, ApJS, 55, 633

- Plunkett, A. L., Arce, H. G., Corder, S. A., et al. 2013, *ApJ*, 774, 22
- Rabli, D., & Flower, D. R. 2010, *MNRAS*, 406, 95
- Robitaille, T., Ginsburg, A., Beaumont, C., Leroy, A., & Rosolowsky, E. 2016, spectral-cube: Read and analyze astrophysical spectral data cubes, , ascl:1609.017
- Sahu, D., Liu, S.-Y., Su, Y.-N., et al. 2019, *ApJ*, 872, 196
- Sakai, N., Sakai, T., Hirota, T., Burton, M., & Yamamoto, S. 2009, *ApJ*, 697, 769
- Sakai, N., Sakai, T., Hirota, T., & Yamamoto, S. 2010, *ApJ*, 722, 1633
- Sakai, N., & Yamamoto, S. 2013, *Chemical Reviews*, 113, 8981
- Sakai, N., Sakai, T., Hirota, T., et al. 2014, *Nature*, 507, 78
- Sakai, N., Oya, Y., López-Sepulcre, A., et al. 2016, *ApJL*, 820, L34
- Schöier, F. L., van der Tak, F. F. S., van Dishoeck, E. F., & Black, J. H. 2005, *A&A*, 432, 369
- Stephens, I. W., Dunham, M. M., Myers, P. C., et al. 2018, *ApJS*, 237, 22
- Stephens, I. W., Bourke, T. L., Dunham, M. M., et al. 2019, *ApJS*, 245, 21
- Tobin, J. J., Looney, L. W., Li, Z.-Y., et al. 2016, *ApJ*, 818, 73
- Tychoniec, L., Tobin, J. J., Karska, A., et al. 2018, *ApJS*, 238, 19
- Tychoniec, L., Manara, C. F., Rosotti, G. P., et al. 2020, arXiv e-prints, arXiv:2006.02812
- Xu, L.-H., & Lovas, F. J. 1997, *Journal of Physical and Chemical Reference Data*, 26, 17
- Xu, L.-H., Fisher, J., Lees, R. M., et al. 2008, *Journal of Molecular Spectroscopy*, 251, 305
- Yang, Y.-L., Evans, Neal J., I., Green, J. D., Dunham, M. M., & Jørgensen, J. K. 2017, *ApJ*, 835, 259
- Yang, Y.-L., Evans, Neal J., I., Smith, A., et al. 2020, *ApJ*, 891, 61
- Zhang, Y., Higuchi, A. E., Sakai, N., et al. 2018, *ApJ*, 864, 76
- Zucker, C., Speagle, J. S., Schlafly, E. F., et al. 2020, *A&A*, 633, A51